Research Square

Preprints are preliminary reports that have not undergone peer review.
They should not be considered conclusive, used to inform clinical practice,
or referenced by the media as validated information.

Adipose extracellular vesicle CFD in growth hormone–driven insulin-dependent hepatic steatosis

Fei Fang

feifang@jiangnan.edu.cn

Jiangnan University https://orcid.org/0009-0007-3270-2452

Peng Wei

Jiangnan University

Junliang Chen

Jiangnan University

Tong Wu

Jiangnan University

Chengying Xu

Jiangnan University

Yajie Wang

Jiangnan University

Yingjie Zhang

Jiangnan University

Kejian Wei

Jiangnan University

Fei Gao

Jiangnan University

Longlong Wang

Jiangnan University

Guocai Duan

Jiangnan University

Rui Zhao

Guangdong University of Technology

Chuang Liu

Jiangnan University

Tao Wan

Zhonghua Lu

Affiliated Hospital of Nantong University

Article

Keywords:

Posted Date: November 19th, 2026

DOI: https://doi.org/10.21203/rs.3.rs-11624174/v1

License: This work is licensed under a Creative Commons Attribution 4.0 International License.
Read Full License

Additional Declarations: There is **NO** Competing Interest.

Adipose extracellular vesicle CFD in growth hormone–driven insulin-dependent hepatic steatosis

Peng Wei[1,2,4], Junliang Chen[1,2,4], Tong Wu[2,4], Chengying Xu[2], Yajie Wang[2], Yingjie Zhang[2], Kejian Wei[2], Fei Gao[2], Longlong Wang[2], Guocai Duan[2], Rui Zhao[2], Chuang Liu[2], Tao Wan[1,2,*], Zhonghua Lu[3,*], Fei Fang[1,2,5,*]

[1]Affiliated Hospital of Jiangnan University, Wuxi 214122, China

[2]Wuxi School of Medicine, Jiangnan University, Wuxi 214122, China

[3]Department of Infectious Diseases, Affiliated Hospital of Nantong University, Nantong, Jiangsu 226001, China

[4]These authors contributed equally

[5]Lead contract

*Correspondence: 8202304002@jiangnan.edu.cn, Lu_z_h@126.com, feifang@jiangnan.edu.cn

Address for lead contract:

Fei Fang, Ph.D., Wuxi School of Medicine, Jiangnan University, 1800 Lihu Road, Wuxi 214122, China.

Abstract

Metabolic dysfunction-associated steatotic liver disease (MASLD) is the most common chronic liver disease, but how adipose tissue dysfunction drives hepatic steatosis remains unclear. Hepatic growth hormone (GH) resistance causes marked lipid accumulation, yet the contribution of adipose GH signaling is unknown. Here we show that adipose tissue–derived complement factor D (CFD) mediates hepatic steatosis in mice with liver-specific GH receptor (*Ghr*) deficiency by comparing liver-specific *Ghr* knockout mice (*L-Ghr* $^{-/-}$) with mice lacking *Ghr* in both liver and adipose tissue. *Cfd* knockout protects against diet-induced obesity-associated steatosis and reduces steatosis in *L-Ghr* $^{-/-}$ mice, identifying CFD as a circulating driver of hepatic steatosis. Mechanistically, Adipose GH signaling promotes PPARγ–STAT5B-dependent *Cfd* transcription, and CFD is packaged into extracellular vesicles that enhance β-cell insulin secretion, promoting hepatic lipogenesis. Inhibiting CFD or its vesicular delivery alleviates steatosis in mice, and circulating vesicle-associated CFD correlates with disease severity in patients with MASLD.

Introduction

Metabolic dysfunction-associated steatotic liver disease (MASLD), the most common chronic liver disorder, has emerged as a major worldwide public health concern, affecting nearly 30% of the global population [1]. MASLD encompasses a progressive spectrum of liver pathology, ranging from hepatic steatosis in metabolic dysfunction-associated fatty liver (MAFL) to metabolic dysfunction-associated steatohepatitis (MASH), which may progress to advanced fibrosis, cirrhosis, and ultimately hepatocellular carcinoma (HCC) [2]. Hepatic metabolic dysregulation in MASLD is intricately linked to dysfunctions in other metabolic organs, including adipose tissue, pancreas, skeletal muscle, and gut, which commonly occurs in the context of obesity, diabetes, dyslipidemia, and hypertension [3,4]. Among these interorgan interactions, crosstalk between adipose tissue and the liver has been implicated in the development of hepatic steatosis and inflammation in MASLD [5]. However, the mechanisms underlying the adipose tissue–liver axis during the progression from MAFL to MASH remain poorly understood.

Hepatic steatosis arises from an imbalance between lipid acquisition and disposal, involving increased hepatic uptake of free fatty acids (FFAs), enhanced *de novo* lipogenesis (DNL), impaired fatty acid oxidation, and reduced lipid export [6-8]. Notably, disruption of the hepatic growth hormone (GH) signaling has been linked to spontaneous hepatic steatosis in mice [9]. Liver-specific deletion of GH receptor (*Ghr*) in *L-Ghr* $^{-/-}$ mice results in pronounced hepatic lipid accumulation [10,11]. Although reduced circulating insulin-like growth factor 1 (IGF-1), a downstream mediator of GH signaling, was initially proposed to contribute to this phenotype, IGF-1 supplementation failed to ameliorate fatty liver, suggesting that additional mechanisms are involved [12]. Intriguingly, adipose tissue-specific *Ghr*-deficiency attenuates high-fat diet-induced hepatic steatosis [13], implicating adipose tissue GH signaling in the regulation of hepatic lipid metabolism. To investigate how adipose tissue contributes to steatosis in the context of hepatic GH resistance, we generated mice with combined adipose tissue- and liver-specific *Ghr* deficiency (*F*/*L-Ghr* $^{-/-}$) and compared their metabolic phenotypes with those of *L-Ghr* $^{-/-}$ mice. Through this approach, we identified complement factor D (CFD), an adipokine also known as adipsin, as a potential mediator of adipose tissue–liver crosstalk in the development of MAFL.

CFD was initially characterized for its role in the alternative pathway of the complement system [14]. Subsequent studies have established its involvement in glucose homeostasis and insulin secretion. CFD promotes the cleavage of complement component C3, generating C3a, which can stimulate insulin secretion from pancreatic islets [15]. Consistently, CFD administration ameliorates hyperglycemia in *db/db* mice [16]. Beyond its role in glucose regulation, CFD has also been implicated in lipid metabolism: it promotes lipogenesis in bone marrow stromal cells, whereas CFD deficiency suppresses intracellular lipid synthesis [17]. These findings raise the possibility that CFD may influence hepatic lipid accumulation not only through its effects on insulin secretion but also through broader metabolic pathways. Moreover, pharmacological inhibition of CFD has been reported to ameliorate hepatic steatosis and hyperglycemia

in experimental models of metabolic liver disease [18]. Thus, CFD may contribute to hepatic steatosis during MASLD development. However, how GH signaling regulates CFD production in adipose tissue and how adipose-derived CFD communicates with the liver to influence hepatic lipid metabolism remain poorly understood.

In this study, using *Cfd* knockout (*Cfd* $^{-/-}$) mice and *L-Ghr* $^{-/-}$ & *Cfd* $^{-/-}$ mice, we further demonstrate that adipose-derived CFD contributes to hepatic steatosis, at least in part, by promoting insulin secretion. Mechanistically, elevated GH signaling in adipose tissue facilitates the cooperation of PPARγ and STAT5B at the *Cfd* promoter, thereby enhancing *Cfd* transcription and CFD production. CFD is subsequently packaged into extracellular vesicles (EVs), which deliver CFD to pancreatic islets and enhance β-cell mitochondrial respiration, ATP production, and Ca^{2+} influx, ultimately potentiating glucose-stimulated insulin secretion. The resulting increase in insulin secretion contributes to hepatic DNL and lipid accumulation. Furthermore, pharmacological inhibition of CFD activity, EVs secretion, or CFD production in adipose tissues effectively alleviates hepatic steatosis in *L-Ghr* $^{-/-}$ mice. Finally, in a clinical cohort, circulating CFD levels—particularly EV-associated CFD—were positively correlated with the severity of hepatic steatosis in patients with MASLD. Collectively, these findings identify an adipose tissue–EV–pancreatic β-cell–liver signaling axis through which CFD links GH signaling in adipose tissue to insulin secretion and hepatic lipid accumulation, highlighting CFD and its EV-mediated delivery as potential diagnostic and therapeutic targets for MASLD.

Results

Adipose tissue GHR ablation alleviates hepatic steatosis in *L-Ghr* $^{-/-}$ mice

To characterize the physiological consequences of *Ghr* deletion in the liver alone or in both liver and adipose tissues, we compared male *L-Ghr* $^{-/-}$ and *F/L-Ghr* $^{-/-}$ mice with *Ghr* $^{f/f}$ as controls. *L-Ghr* $^{-/-}$ mice developed hepatomegaly accompanied by robust hepatic triglyceride accumulation, as reflected by larger and pallid livers within comparable body size (**Fig. 1a**), an increased liver-to-body weight ratio (**Fig. 1b**) and elevated intrahepatic triglyceride (TG) levels (**Fig. 1c**). Histological examinations revealed severe hepatic steatosis, abundant lipid droplet deposition, and enhanced collagen deposition in *L-Ghr* $^{-/-}$ mice liver tissues, together with elevated plasma alanine aminotransferase (ALT) and aspartate aminotransferase (AST) indicating hepatocellular injury (**Fig. 1d, e, f**). Importantly, these pathological manifestations of liver steatosis were largely prevented in *F/L-Ghr* $^{-/-}$ double-knockout mice. In agreement with results in male mice, female *L-Ghr* $^{-/-}$ mice exhibited increased hepatic triglyceride content, evident lipid droplet deposition in liver sections, and higher plasma ALT and AST levels than female littermate controls. Consistently, these pathological changes were alleviated in female *F/L-Ghr* $^{-/-}$ mice (Fig. S1a-d).

At the systemic level, *L-Ghr* $^{-/-}$ mice did not show hypertriglyceridemia (**Fig. 1g**), and circulating free fatty acids (FFA) (**Fig. 1i**) were not increased. Lipidomic analysis further demonstrated no disturbances in plasma triglyceride and FFA profiles across various acyl-chain lengths among the three genotypes (**Fig. 1h, j**). Since food intake

was comparable among all three genotypes, the metabolic and hepatic phenotypes were independent of feeding behavior (**Fig. 1k**). We additionally monitored the respiratory quotient to evaluate whole-body substrate utilization, and no differences were observed among the three genotypes (**Fig. 1l**). Collectively, these data suggest that the alleviation of hepatic steatosis by concomitant adipose GHR deletion in *L-Ghr* $^{-/-}$ mice, is unlikely to be explained by altered feeding behavior, systemic lipid availability, or fat utilization; instead, it may involve the regulation of hepatic lipogenesis and/or lipid uptake.

Adipose GHR deletion diminishes insulin-driven lipogenesis in *L-Ghr* $^{-/-}$ mice

To further dissect the mechanisms underlying hepatic phenotypes caused by the loss of liver or/and adipose GHR, we performed RNA sequencing (RNA-seq) on the livers of *Ghr* $^{f/f}$, *L-Ghr* $^{-/-}$, and *F/L-Ghr* $^{-/-}$ mice. KEGG enrichment analysis revealed that the substantial transcriptional alterations in both *Ghr* $^{f/f}$ vs *L-Ghr* $^{-/-}$ and *F/L-Ghr* $^{-/-}$ vs *L-Ghr* $^{-/-}$ comparisons were strongly enriched in fatty acid metabolic process (**Fig. 2a**). Pairwise differential expression analysis identified 338 genes upregulated in *L-Ghr* $^{-/-}$ compared with *Ghr* $^{f/f}$ and 108 genes upregulated compared with *F/L-Ghr* $^{-/-}$, with 68 genes overlapping (**Fig. 2b**). Among these overlapping genes, lipogenesis-related genes were involved (**Fig. 2b**). Moreover, gene set enrichment analysis (GSEA) demonstrated enrichment of genes related to lipogenesis in *L-Ghr* $^{-/-}$ mice (**Fig. 2c**). The heatmap showed the top 27 overlapping significantly differentially expressed genes, including several key lipogenic genes (**Fig. 2d**). RT-qPCR validated that representative lipogenic genes were markedly upregulated in the livers of *L-Ghr* $^{-/-}$ mice and partially normalized in *F/L-Ghr* $^{-/-}$ mice, whereas no changes were observed in the expression of genes involved in fatty acid uptake, oxidation, or VLDL secretion (**Fig. 2e**). Immunoblotting further confirmed that hepatic abundances of lipogenic effectors ACC1, FAS, SCD1 and SREBP1 were increased in *L-Ghr* $^{-/-}$ mice but lowered in *F/L-Ghr* $^{-/-}$ mice (**Fig. 2f**). In female mice, similar changes in lipogenic gene expression were observed at both RNA and protein levels across the three genotypes (Fig. S1e-f).

To determine whether enhanced hepatic lipogenesis is associated with insulin resistance, glucose tolerance tests (GTTs) and insulin tolerance tests (ITTs) were performed. Interestingly, *L-Ghr* $^{-/-}$ mice exhibited improved glucose tolerance but impaired insulin sensitivity, whereas *F/L-Ghr* $^{-/-}$ mice showed mildly defective glucose tolerance but normal insulin sensitivity (**Fig. 2g, h**). These results suggest that *L-Ghr* $^{-/-}$ mice may have compensatory hyperinsulinemia that preserves glucose tolerance despite insulin resistance, whereas this compensation appears to be absent in *F/L-Ghr* $^{-/-}$ mice. In other words, the elevated endogenous insulin in *L-Ghr* $^{-/-}$ mice may preserve glucose-lowering capacity and offset the reduced response to exogenous insulin, whereas this compensatory response appears to be absent in *F/L-Ghr* $^{-/-}$ mice. Although circulating growth hormone (GH) levels were elevated in *L-Ghr* $^{-/-}$ and *F/L-Ghr* $^{-/-}$ mice, with no differences between each other, high plasma insulin levels were nevertheless present only in *L-Ghr* $^{-/-}$ mice, not in *F/L-Ghr* $^{-/-}$ mice (**Fig. 2i, j**). Similar changes in plasma insulin levels were detected across the three female genotypes (Fig. S1g). Indeed, the elevated insulin levels may explain the increased hepatic lipogenesis in *L-Ghr* $^{-/-}$ mice. Given the elevated circulating insulin levels, we next examined

pancreatic islet morphology. Histological and immunohistochemical analyses revealed an increased number of islets, but not islet enlargement, in *L-Ghr* $^{-/-}$ mice, leading to increased insulin production; however, this phenotype was reversed in *F/L-Ghr* $^{-/-}$ mice (**Fig. 2k, l**). Together, these findings suggest that elevated GH acts on adipose tissue to indirectly stimulate insulin production in pancreatic islet, thereby promoting hepatic lipogenesis, an effect that is ameliorated by concomitant deletion of GHR in adipose tissue.

Adipokine CFD elevation stimulates insulin secretion and hepatic steatosis in *L-Ghr* $^{-/-}$ mice

To find out the secreted effector from adipose tissue in *L-Ghr* $^{-/-}$ mice, we used a plasma proteome profiler assay to screen for circulating pathogenic factors. Chip screening identified 4 secretory factors that were strongly upregulated in *L-Ghr* $^{-/-}$ mice and normalized in *F/L-Ghr* $^{-/-}$. In particular, one of these factors was CFD, an adipokine. (**Fig. 3a**). Plasma immunoblotting and ELISA further confirmed the corresponding changes in CFD levels among these mice (**Fig. 3b, c**), yet circulating levels of C3a, a downstream product of C3 cleavage by CFD, remained unchanged (**Fig. 3d**), suggesting that C3a is unlikely to mediate the pathological changes. Further analyses demonstrated that *Cfd* mRNA and protein levels were markedly increased in multiple white and brown adipose depots of *L-Ghr* $^{-/-}$ mice but profoundly downregulated in *F/L-Ghr* $^{-/-}$ mice, as validated by RT-qPCR, Western blot, and immunohistochemistry (**Fig. 3e, f, g**). Moreover, in contrast to its abundant expression in adipose tissue, CFD expression was undetectable in the liver, indicating that hepatic lipogenesis is probably not dependent on locally produced CFD (Fig. S2a). Next, treatment of hepatocytes with CFD had no direct effect on the expression of key lipogenic genes, whereas insulin efficiently induced these genes (Fig. S2b, c), suggesting that adipokine CFD promotes hepatic steatosis indirectly through insulin stimulation.

To establish the causal role of adipose-derived CFD in driving the metabolic pathologies, we employed ap2-*Cfd* shRNA AAV and specifically injected it into abdominal and subcutaneous adipose depots of *L-Ghr* $^{-/-}$ mice (**Fig. 3h**). After confirming that CFD protein levels were efficiently knocked down in adipose tissue, we found that both plasma CFD and insulin levels were significantly decreased compared with those in the control shRNA AAV group (**Fig. 3i, j**). Consistently, compensatory pancreatic islet hyperplasia was mitigated following *Cfd* knockdown (**Fig. 3k**). At the hepatic level, adipose-specific ablation of *Cfd* repressed the over-activated hepatic lipogenic transcriptional program at both mRNA and protein levels (**Fig. 3l, m**). Histological assessment and biochemical measurement demonstrated alleviated lipid droplet deposition and reduced hepatic triglyceride content in ap2-*Cfd* shRNA injected *L-Ghr* $^{-/-}$ mice (**Fig. 3n, o**). To further test whether hepatic insulin signaling mediates the pathogenic phenotypes observed in *L-Ghr* $^{-/-}$ mice, we performed liver-specific knockdown of insulin receptor (*Insr)* using TBG-AAV-delivered shRNA. Multiple shRNA candidates were first validated for efficient silencing of INSR-A and INSR-B isoforms in Hepa 1-6 cells, and the most effective one was selected to construct AAV shRNA (Fig. S3a). *In vivo* fluorescence imaging

verified successful liver-targeted transduction after AAV administration (Fig. S3b). In *L-Ghr* $^{-/-}$ mice, hepatic *Insr* knockdown did not change circulating CFD concentration, and produced only marginal alterations in plasma insulin levels (Fig. S3c). In contrast, elevated hepatic RNA and protein levels of lipogenic genes were rescued by *Insr* silencing (Fig. S3d, e). Moreover, histological staining and hepatic TG measurement demonstrated that knockdown of hepatic *Insr* alleviated lipid accumulation in the liver (Fig. S3f, g). Collectively, these data support a model in which adipose tissue-derived CFD acts as the major upstream circulating effector that promotes insulin secretion and induces insulin-driven hepatic steatosis in *L-Ghr* $^{-/-}$ mice.

CFD deletion ameliorates insulin-induced hepatic steatosis in DIO and *L-Ghr* $^{-/-}$ mice

To further validate the pathogenic function of CFD genetically, global-*Cfd*-knockout mice were generated and studied. Immunoblotting first confirmed complete deletion of CFD protein in adipose tissue of *Cfd* $^{-/-}$ mice (Fig. S4a). Under normal chow diet feeding, no differences were observed in plasma insulin levels, pancreatic islet histology, or islet size between WT and *Cfd* $^{-/-}$ mice (Fig. S4b-d). Similarly, hepatic triglyceride levels and the expression of key hepatic lipogenic proteins were indistinguishable between the two groups (Fig. S4e, f). However, starting from 3 weeks of HFD feeding, *Cfd* $^{-/-}$ mice gained less body weight than WT mice (**Fig. 4a**). After 6 weeks of HFD feeding, plasma insulin levels in WT mice were elevated to approximately 4 ng/ml, whereas those in *Cfd* $^{-/-}$ mice were lower, at around 2 ng/ml, accompanied by low plasma CFD levels in *Cfd* $^{-/-}$ mice (**Fig. 4b, c**). Pancreatic histological analyses revealed that the HFD-induced increase in islet number was attenuated in *Cfd* $^{-/-}$ mice (**Fig. 4d**), and HFD-triggered compensatory islet hyperplasia was also reduced in these mice (**Fig. 4e**). Moreover, HFD fed *Cfd* $^{-/-}$ mice exhibited impaired glucose tolerance but improved insulin sensitivity (**Fig. 4f, g**), suggesting that the impaired glucose tolerance may be attributable to impaired insulin secretion rather than insulin resistance. In addition, *Cfd* $^{-/-}$ mice showed reduced hepatic triglyceride deposition and attenuated fat accumulation (**Fig. 4h, i**). Consistently, RT-qPCR and immunoblotting demonstrated that HFD-induced activation of the hepatic lipogenic program was strongly suppressed in the livers of *Cfd* $^{-/-}$ mice (**Fig. 4j, k**).

We next generated *L-Ghr* $^{-/-}$*&Cfd* $^{-/-}$ double-knockout mice to investigate whether *Cfd* deletion could counteract the phenotypes in *L-Ghr* $^{-/-}$ mice. Complete CFD protein ablation was confirmed in adipose tissues of double-knockout mice (**Fig. 4l**). As a result, plasma CFD and insulin levels markedly fell in *L-Ghr* $^{-/-}$*&Cfd* $^{-/-}$ mice (**Fig. 4m**), along with reduced pancreatic islet number in histological analyses (**Fig. 4n**). In the liver, *Cfd* deletion significantly alleviated fat accumulation with reduced hepatic TGs content (**Fig. 4o, p**). Mechanically, *Cfd* deletion suppressed the upregulated lipogenic genes in *L-Ghr* $^{-/-}$ mice at both RNA and protein levels (**Fig. 4q, r**). Taken together, these genetic loss-of-function data demonstrate that CFD is a necessary mediator linking hyperinsulinemia, increased islet number, and hepatic steatosis in both DIO and *L-Ghr* $^{-/-}$ mice.

PPARγ-STAT5 interaction activates *Cfd* transcription

Having established that upregulated CFD from adipose tissue mediates metabolic pathology, we next sought to dissect the upstream transcriptional mechanism underlying the aberrant expression of *Cfd*. Aaron et al. reported that *Cfd* is regulated by PPARγ [17]. In addition, STAT5 is an important downstream activator of GH signaling. Therefore, we first explored the potential role of PPARγ and STAT5 in *Cfd* transcription. Importantly, adipose PPARγ expression correlated with CFD levels among *Ghr* $^{f/f}$, *L-Ghr* $^{-/-}$, and *F/L-Ghr* $^{-/-}$ mice (**Fig. 5a**). *Cfd* mRNA and protein levels gradually increased during adipogenic differentiation *in vitro* (Fig. S5a, b). During differentiation, PPARγ expression were progressively upregulated, accompanied by increased STAT5 protein levels (**Fig. 5b**). Notably, treatment with T0070907, a PPARγ antagonist, or STAT5-IN-1, a STAT5 inhibitor, profoundly suppressed CFD expression at both RNA and protein levels (**Fig. 5c, d**). Furthermore, *Pparγ* knockdown by shRNA consistently reduced CFD expression (**Fig. 5e**, S5c). To clarify which STAT5 isoform, STAT5A or STAT5B, is involved in this process, we individually silenced each isoform using siRNA. In both differentiation of primary adipocytes and 3T3-L1 cells, knockdown of *Stat5b*, rather than *Stat5a*, distinctly downregulated CFD expression (**Fig. 5f**, S5d).

To further investigate how PPARγ and STAT5 regulate the *Cfd* promoter, we performed CUT&Tag analysis, which revealed prominent co-occupancy of PPARγ and STAT5 at the *Cfd* promoter locus, with PPARγ showing greater enrichment than STAT5 (**Fig. 5g**). Motif analysis speculated that putative adjacent binding sites for PPARγ and STAT5 within *Cfd* promoter (**Fig. 5h, i**), suggesting that PPARγ may have a greater propensity than STAT5 to bind to the *Cfd* promoter. Next, truncated-promoter luciferase assays further mapped the PPARγ-responsive element to the -550 bp ~ -100bp region of the *Cfd* promoter (**Fig. 5j**). The antagonist of PPARγ blocked PPARγ-induced *Cfd* promoter activity (**Fig. 5k**), and correspondingly reduced CFD protein levels (Fig. S5e). Conversely, the agonist of PPARγ further potentiated *Cfd* promoter activity under PPARγ overexpression (**Fig. 5k**). Next, silencing of *Stat5b*, but not *Stat5a*, significantly reduced *Cfd* promoter activity. Likewise, combined knockdown of *Stat5b* and *Stat5a* did not additionally decrease CFD protein levels compared with *Stat5b* silencing alone (Fig. S5f), suggesting that STAT5B, rather than STAT5A, predominantly contributes to the transcriptional regulation of *Cfd*. Interestingly, *Stat5b* overexpression paradoxically suppressed *Cfd* promoter activity (**Fig. 5l**). This inhibitory effect may be attributable to the accumulation of non-phosphorylated, transcriptionally inactive STAT5B, which could competitively interfere with the binding or transcriptional activity of phosphorylated STAT5B at the *Cfd* promoter. ChIP-qPCR further confirmed the recruitment of both STAT5 and PPARγ to the *Cfd* promoter (**Fig. 5m**). Moreover, co-immunoprecipitation assays demonstrated that PPARγ interacted with both STAT5A and STAT5B (**Fig. 5n**, S5g), suggesting the PPARγ may cooperate with STAT5 to regulate *Cfd* transcription. However, STAT5B but not STAT5A was required for PPARγ-induced CFD expression (**Fig. 5o**), and the phosphorylated, transcriptionally active form of STAT5B may be necessary for PPARγ-mediated upregulation of CFD (**Fig. 5p**). Taken together, these data support a working model in which activated STAT5B cooperates with PPARγ through their physical interaction to synergistically

enhance *Cfd* transcription.

GH-activated STAT5B–PPAR-γ interaction drives PPAR-γ nuclear translocation and subsequent CFD upregulation

We next investigated how GH facilitates STAT5B-PPARγ-dependent upregulation of CFD. Dual-luciferase assays first revealed that GH augmented STAT5B and PPARγ-mediated synergistic activation of the *Cfd* promoter, while mildly attenuating the transcriptional activation mediated by STAT5A and PPARγ (**Fig. 6a**). Co-immunoprecipitation results showed that GH markedly reinforced the interaction between STAT5B and PPARγ, but not between STAT5A and PPARγ, in a dose-dependent manner (**Fig. 6b, c**). Importantly, *Ghr* knockdown efficiently blunted GH induced CFD expression, accompanied by a reduction in STAT5 protein levels (**Fig. 6d**). Consistently, silencing of *Stat5b*, but not *Stat5a,* abolished the upregulation of CFD in response to GH (**Fig. 6e**), further supporting a critical role for STAT5B in mediating GH-induced CFD expression. Notably, cellular fractionation assays demonstrated that GH promoted nuclear enrichment of STAT5B in the form of phosphorylation, and along with PPARγ (**Fig. 6f**), suggesting GH may facilitate PPARγ nuclear translocation through p-STAT5B-driven interaction. Next, knockdown of *Stat5b* indeed reduced nuclear accumulation of PPARγ stimulated by GH, whereas STAT5B overexpression strengthened nuclear localization of PPARγ in response to GH, as shown in immunofluorescence staining (**Fig. 6g, h**). ChIP-qPCR further illustrated that GH substantially increased STAT5B and PPARγ chromatin occupancy on the *Cfd* promoter; such enhanced binding was eliminated by *Stat5b* knockdown (**Fig, 6i, j**). Consistently, PPARγ knockdown largely abolished the increase in CFD induced by STAT5B overexpression under GH treatment (**Fig. 6k**). Collectively, these data demonstrates that GH promotes STAT5B activation and its interaction with PPARγ, facilitating PPARγ nuclear translocation and the co-recruitment of STAT5B and PPARγ to the *Cfd* promoter, thereby enhancing *Cfd* transcription and CFD expression.

CFD in EVs acts on islets to stimulate insulin secretion

Having elucidated the mechanism underlying GH-mediated regulation of CFD, we next investigated its downstream effects on insulin secretion. Given that plasma C3a levels remained unchanged (**Fig. 3d**), we examined whether CFD exerts a direct pro-insulinotropic effect. To this end, recombinant CFD was applied to primary islets during glucose-stimulated insulin secretion (GSIS) assays. However, exogenous CFD failed to directly stimulate insulin secretion from primary islet cells (**Fig. 7a**). Zhang et. al. reported that CFD is enriched in adipose tissue-derived exosomes [19], prompting us to investigate whether CFD is carried by circulating extracellular vesicles (EVs) and acts on pancreatic β-cells. We sequentially isolated EVs from mouse plasma by differential ultracentrifugation in two successive steps, yielding crude EVs (1st EVs) and refined EVs (2nd EVs) [20] (**Fig. 7b**). Nanoparticle tracking analysis (NTA) showed typical EVs size distribution in plasma-derived EVs from $Ghr^{f/f}$, $L\text{-}Ghr^{-/-}$, and $F/L\text{-}Ghr^{-/-}$ mice, with no significant differences among them (**Fig. 7c**), and transmission electron microscopy (TEM) confirmed the characteristic cup-shaped morphology of the isolated EVs (**Fig.**

7d). Next, immunoblotting importantly revealed that CFD protein was profoundly enriched in both 1st and 2nd EVs isolated from *L-Ghr* $^{-/-}$ plasma compared with those from *Ghr* $^{f/f}$, whereas CFD enrichment in EVs was reduced to near-baseline levels in *F/L-Ghr* $^{-/-}$ mice (**Fig. 7e**). In isolated primary islet, plasma-derived EVs from *L-Ghr* $^{-/-}$ mice increased insulin secretion and elevated intracellular ratio of ATP/ADP, whereas these effects were largely restored to baseline following treatment with plasma-derived EVs from *F/L-Ghr* $^{-/-}$ mice (**Fig. 7f**). Consistently, calcium imaging and qualificative analysis revealed that EVs from *L-Ghr* $^{-/-}$ mice stimulated the signal for following insulin secretion, whereas EVs from *F/L-Ghr* $^{-/-}$ mice blocked these changes (**Fig. 7g**). Furthermore, after confirming successfully uptake of these EVs by islet β cell line (Fig. S6a), we found that EVs derived from *L-Ghr* $^{-/-}$ mice similarly enhanced insulin secretion, the cellular ATP, and calcium influx (Fig. S6b-d). Notably, dynamic calcium influx also revealed higher peak Ca^{2+} response in β–cells treated with EVs from *L-Ghr* $^{-/-}$ mice (Fig. S6e), supporting enhanced capacity to stimulate β-cell secretory activity. To directly determine whether these effects were attributable to CFD cargo within EVs, we generated CFD-loaded milk-derived EVs via electroporation (**Fig. 7h**). NTA and TEM showed the undistinctive size and number between control and CFD loading EVs (**Fig. 7i, j**). Moreover, DLS analysis revealed an increased hydrodynamic diameter, accompanied by an altered zeta potential, in CFD-loaded EVs compared with control EVs, indicating changes in their physicochemical properties following CFD loading (Fig. S7a, b). Importantly, ELISA further confirmed the successful incorporation of CFD cargo into the EVs (Fig. S7c). Notably, CFD-loaded EVs treatment potentially enhanced insulin secretion, intracellular ATP level and calcium influx in dose dependent manner (Fig. S7d). Next, in isolated primary islets exposed to high glucose, treatment with CFD-loaded EVs markedly enhanced insulin secretion, the intracellular ATP/ADP ratio, and Ca^{2+} influx. However, these effects were not observed under low-glucose conditions (**Fig. 7k**). Consistently, following confirmation of EVs uptake (Fig. S7e), similar effects were observed in Min6 cells (Fig. S7f). Moreover, treatment with CFD-loaded EVs profoundly enhanced the dynamic Ca^{2+} influx in the human pancreatic β-cell line 1.1B4 (Fig. S7g). In addition, to further assess the effects of CFD-loaded EVs on mitochondrial function, we measured oxygen consumption using the Seahorse XF Pro extracellular flux analyzer. CFD-loaded EVs treatment significantly increased the oxygen consumption rate (OCR) in Min6 cells (**Fig. 7l, m**), indicating enhanced mitochondrial respiratory activity that may contribute to the increased ATP production and insulin secretion.

To further validate these findings *in vivo*, CFD-loaded EVs were administered by in situ injection (**Fig. 7n**), following the surgical procedure described by Ruo Ran et al [21]. Immunofluorescence analysis confirmed that CFD-loaded EVs were internalized by pancreatic β-cells following in situ delivery (Fig. S7h). Notably, circulating insulin levels increased rapidly following administration of CFD-loaded EVs (Fig. S7i). Consistently, confocal imaging of pancreatic islets revealed a specific increase in insulin staining, whereas glucagon staining remained largely unchanged (**Fig. 7o**). Importantly, systemic administration of CFD-loaded EVs significantly increased plasma insulin levels in recipient mice (**Fig. 7p**), providing direct *in vivo* evidence that

EV-encapsulated CFD promotes pancreatic β-cell insulin secretion. However, in hepatocytes, CFD-loaded EVs were similarly taken up but failed to induce the expression of lipogenic genes in both mouse and human hepatocyte cell lines, ruling out its direct role on stimulation of hepatic lipogenesis (Fig. S7j, k). Together, these findings demonstrate that EVs-encapsulated CFD is efficiently taken up by pancreatic β-cells, where it enhances mitochondrial respiration and ATP production, thereby promoting Ca^{2+} influx and insulin secretion, which subsequently drives hepatic DNL.

Multi-level CFD inhibition attenuates hepatic steatosis in *L-Ghr*$^{-/-}$ mice

To explore potential therapeutic strategies, we performed *in vivo* pharmacological interventions in *L-Ghr*$^{-/-}$ mice by targeting CFD activity, EVs secretion or STAT5B activation, thereby pharmacologically disrupting distinct steps of the GH-STAT5B-CFD-EVs signaling axis. The *in vivo* administration protocol for the CFD-specific inhibitor FD-IN-1 [22] by local injection into adipose tissue is illustrated in the model (**Fig. 8a**). Following FD-IN-1 administration every two days for 2 weeks, CFD expression in white adipose tissue remained unchanged compared with vehicle-treated mice (**Fig. 8b**). Consistently, plasma CFD levels were comparable between the two groups. In contrast, plasma insulin levels were significantly reduced following FD-IN-1 treatment (**Fig. 8c**), suggesting that pharmacological inhibition of CFD activity attenuates its insulinotropic effect. Histological analyses of the pancreas further revealed a reduction in the number of pancreatic islets in FD-IN-1-treated mice (**Fig. 8d**). Next, FD-IN-1 treatment significantly alleviated hepatic lipid accumulation and reduced hepatic TG content in mice (**Fig. 8e, f**). Consistently, key regulators of hepatic DNL, including ACC1, FAS, SCD1, and SREBP1, were markedly downregulated at both the mRNA and protein levels, supporting a role for CFD activity in promoting hepatic lipogenesis (**Fig. 8g, h**).

We next investigated whether pharmacological inhibition of EVs secretion could recapitulate the metabolic effects of CFD inhibition by treating *L-Ghr*$^{-/-}$ mice with exosome secretion inhibitor GW4869 (**Fig. 8i**). Following two weeks of GW4869 administration, CFD protein expression in adipose tissue remained unchanged compared with that in vehicle-treated mice (**Fig. 8j**). Notably, however, both circulating CFD and insulin levels were significantly reduced following GW4869 treatment (**Fig. 8k**), consistent with impaired EV-mediated release of CFD. In parallel, histological analyses revealed a reduction in the number of pancreatic islets in GW4869-treated mice (**Fig. 8l**). Importantly, GW4869 treatment also markedly alleviated hepatic lipid accumulation and reduced hepatic TG content (**Fig. 8m, n**), accompanied by consistent downregulation of key hepatic lipogenic genes and proteins (**Fig. 8o, p**). Finally, given that activated STAT5B promotes CFD expression, we next investigated whether pharmacological inhibition of STAT5 signaling could ameliorate the metabolic phenotype in *L-Ghr*$^{-/-}$ mice. Mice received in situ administration of the STAT5 inhibitor STAT-IN-1 into adipose tissue (**Fig. 8q**), resulting in markedly reduced adipose CFD production (**Fig. 8r**) and concomitant decreases in circulating CFD and insulin levels (**Fig. 8s**). Consistently, pancreatic histological analyses demonstrated a significant decrease in islet number following STAT-IN-1 treatment (**Fig. 8t**). Importantly, STAT5

inhibition also markedly alleviated hepatic steatosis in *L-Ghr* $^{-/-}$ mice, as evidenced by reduced hepatic lipid accumulation and TG content (**Fig. 8u, v**), accompanied by reversal of the excessive activation of hepatic lipogenic pathway (**Fig. 8w, x**). Collectively, these pharmacological interventions provide convergent evidence that the adipocytic STAT5B–CFD–EVs axis promotes insulin secretion and contributes to hepatic lipid accumulation, supporting a STAT5B–CFD–EVs–insulin signaling cascade in the development of hepatic steatosis.

Circulating CFD correlates positively with hepatic steatosis in MASLD patients

Given the pathogenic role of CFD in promoting insulin secretion and contributing to hepatic steatosis in mouse models, we next investigated whether circulating CFD, particularly EV-associated CFD, could serve as a clinical biomarker for MASLD. Histological analysis of human liver specimens confirmed progressive hepatic lipid accumulation across the normal, moderate-steatosis, and severe-steatosis groups (**Fig. 9a**). Consistently, plasma levels of ALT, insulin, and CFD were significantly elevated with increasing severity of hepatic steatosis (**Fig. 9b, c, d**). In addition to the positive correlation between plasma ALT and insulin levels (**Fig. 9e**), correlation analyses revealed strong positive correlations between circulating CFD and both ALT and insulin levels (**Fig. 9f**). Receiver operating characteristic (ROC) curve analysis showed that plasma CFD outperformed plasma insulin and approached plasma ALT in identifying patients with severe hepatic steatosis, whereas a combined three-biomarker panel further improved diagnostic sensitivity and specificity (**Fig. 9g**).

We next investigated the distribution of CFD in circulating EVs isolated from human plasma samples. NTA and TEM confirmed the successful isolation of intact EVs from human plasma (**Fig. 9h, i**). Immunoblotting revealed that CFD levels within the EV fraction were markedly increased in patients with severe hepatic steatosis (**Fig. 9j**). Notably, the proportion of EVs-associated CFD relative to total circulating CFD was significantly higher in the severe-steatosis group, whereas CFD levels in the EV-depleted supernatant remained comparable among the three groups (**Fig. 9k**). Taken together, these clinical cohort findings suggest that circulating EV-associated CFD may represent a promising non-invasive biomarker for assessing hepatic steatosis in patients with MASLD.

Discussion

In this study, we identify an adipose tissue–EV–pancreas–liver signaling axis through which GH-regulated CFD contributes to hepatic steatosis. We demonstrate that GH promotes *Cfd* transcription through STAT5B and PPARγ in adipose tissue, while EV-associated CFD enhances pancreatic β-cell mitochondrial respiration, ATP production, Ca^{2+} responses, and GSIS. The resulting increase in insulin secretion may promote hepatic DNL and lipid accumulation (**Fig. 10**). Notably, CFD-loaded EVs were taken up by hepatocytes but did not induce lipogenic gene expression in the cell models examined, supporting an indirect mechanism in which CFD influences hepatic lipid metabolism through pancreatic insulin secretion. These findings reveal a potential role

for EV-mediated CFD delivery in interorgan metabolic communication.

Previous studies have implicated CFD in hepatic lipid metabolism and metabolic dysfunction. CFD inhibition has been reported to alleviate hepatic steatosis in experimental models [18], while other work suggests that CFD can influence systemic metabolism through signaling pathways involving adipose tissue [23]. These findings indicate that CFD may regulate lipid metabolism through multiple tissue-dependent mechanisms. Our study extends this knowledge by identifying adipose-derived CFD as a mediator linking hepatic GH resistance to pancreatic insulin secretion and hepatic lipid accumulation. Rather than excluding potential direct hepatic effects of CFD in other contexts, our findings reveal an additional, indirect mechanism involving EV-mediated communication between adipose tissue and pancreatic islets.

Mechanistically, our findings identify a GH–STAT5B–PPARγ pathway that regulates adipose CFD production. GH enhanced STAT5B–PPARγ interaction, promoted PPARγ nuclear localization, and increased the recruitment of both transcription factors to the *Cfd* promoter. STAT5B, but not STAT5A, was required for the full transcriptional response. These results suggest that GH signaling regulates adipose endocrine output through coordinated transcriptional control of *Cfd*. These data also highlight the potential importance of tissue-specific GH responsiveness in metabolic regulation, whereby impaired hepatic GH signaling may coexist with GH-dependent signaling in adipose tissue that promotes CFD production and downstream metabolic effects.

Previous work by Lo and colleagues established that CFD promotes β-cell function partly through C3a generation and C3a receptor (C3aR) signaling, enhancing insulin secretion and β-cell metabolic activity [15,16]. Subsequent studies have shown that adipocyte-derived EVs can regulate β-cell survival and function [24] and transport insulinotropic protein cargo to pancreatic β cells [25]. Building on these findings, we demonstrate that CFD-containing EVs enhance β-cell mitochondrial respiration, ATP production, Ca^{2+} responses, and insulin secretion, whereas recombinant CFD alone did not stimulate GSIS under our experimental conditions (**Fig. 7a**). This difference suggests that the biological effects of CFD may depend on its delivery context. EVs may facilitate the transport or presentation of CFD to pancreatic islets, providing an additional mechanism through which adipose tissue regulates β-cell function. However, unchanged circulating C3a levels (**Fig. 3d**) do not completely exclude local complement activation, and further experiments are needed to determine whether EV-associated CFD acts through canonical C3a/C3aR signaling [26], an alternative pathway, or both.

The functional consequences of this pathway extend to hepatic lipid metabolism. In our mouse models, genetic or pharmacological disruption of CFD activity, EV secretion, or STAT5 signaling reduced circulating insulin and attenuated hepatic lipid accumulation, accompanied by decreased expression of lipogenic genes and proteins. Together with the absence of lipogenic gene induction in CFD-EV-treated hepatocytes, these findings support a model in which EV-associated CFD promotes hepatic steatosis primarily through β-cell stimulation and insulin-mediated lipogenesis. Insulin is an established regulator of hepatic DNL, in part through pathways involving SREBP1 and fatty acid synthesis enzymes [27]. Although the pharmacological interventions used here

may have additional effects, their convergent outcomes support a functional contribution of the adipose CFD–EV–insulin axis to hepatic lipid accumulation. More broadly, our findings suggest that EV-mediated protein transport represents a mechanism through which adipose tissue can influence liver metabolism without directly activating lipogenic programs in hepatocytes.

Our findings may also have implications for lean MASLD [28]. Although MASLD is frequently associated with obesity, hepatic steatosis also occurs in individuals without obesity, suggesting that factors beyond total adiposity contribute to disease susceptibility [29]. The GH–IGF-1 axis regulates body composition and lipid metabolism, and a systematic review and meta-analysis linked GH deficiency to an increased prevalence of MASLD [30,31]. In addition, a randomized clinical trial found that GH administration reduced intrahepatic lipid content in adults with overweight or obesity and MASLD [32]. However, GH infusion has also been shown to rapidly induce basal hyperinsulinemia [33,34], which could favor hepatic DNL and contribute to hepatic lipid accumulation. These seemingly opposing effects highlight the complex role of GH in hepatic lipid homeostasis and raise the possibility that altered GH signaling may contribute to metabolic disturbances, including insulin resistance, in lean MASLD. Our results raise the possibility that tissue-specific differences in GH responsiveness could contribute to hepatic steatosis even in the absence of overt obesity. In our models, impaired hepatic GH signaling was associated with enhanced adipose CFD-related signaling, potentially linking altered GH responses to increased insulin secretion and hepatic DNL. If this mechanism also operates in lean MASLD, the GH–CFD–EV–insulin axis could help explain hepatic lipid accumulation in a subset of patients without substantial excess body weight. This hypothesis warrants direct investigation in well-characterized lean MASLD cohorts. Comparing GH–IGF-1 parameters, circulating CFD, and EV-associated CFD between lean and obesity-associated MASLD may help identify distinct metabolic subgroups and inform future therapeutic strategies targeting CFD production, EV-mediated delivery, or downstream signaling. However, our findings do not establish that this pathway drives lean MASLD in humans, nor do they justify GH manipulation as a treatment without further evidence.

Consistent with our experimental findings, circulating CFD levels in our clinical cohort increased with hepatic steatosis severity and correlated positively with insulin and ALT levels. CFD was enriched in the plasma EV fraction in patients with severe steatosis, whereas CFD levels in the EV-depleted supernatant remained relatively unchanged. These findings suggest that EV-associated CFD may provide information beyond total circulating CFD and could represent a candidate biomarker for assessing hepatic steatosis severity. Further validation in independent cohorts, particularly those including well-characterized lean MASLD populations, is required to establish its clinical utility and determine whether it improves disease assessment beyond existing biomarkers. Several questions remain unresolved. The molecular mechanism by which EV-associated CFD stimulates insulin synthesis or secretion in β-cells requires further investigation. In particular, it remains unclear whether CFD acts at the cell surface, is released from EVs extracellularly, or enters β-cells to engage intracellular targets.

In conclusion, our study identifies a GH-regulated adipose tissue–EV–pancreas–liver

signaling axis through which CFD contributes to hepatic steatosis. By linking EV-associated CFD to β-cell metabolic activity and insulin secretion, we extend previous findings on the CFD–C3a pathway and identify a potential mechanism connecting adipose endocrine signaling to hepatic DNL. These findings also provide a rationale for investigating EV-associated CFD as a potential biomarker and therapeutic target in MASLD, particularly in patients with lean MASLD, in whom the mechanisms underlying hepatic steatosis remain incompletely understood.

Methods

Human samples

Plasma samples used in this study were collected from 31 patients with MASLD and 18 healthy individuals without MASLD at the Fifth People's Hospital of Wuxi, which is affiliated with Jiangnan University. Paraffin-embedded sections of human liver tissue were also obtained from the same institution. Liver specimens were obtained from the same 31 patients with MASLD and biopsy-proven hepatic steatosis; of these, 21 had moderate steatosis (>33% but <66% fat accumulation) and 10 had severe steatosis (>66% fat accumulation). Histological evaluation excluded autoimmune liver disease and inherited metabolic liver disease. Normal liver samples were obtained from liver resections showing no microscopic pathological features of hepatic steatosis. Written informed consent was obtained from all participants before sample collection. All procedures involving human samples were approved by the Ethics Committee of Jiangnan University (Approval No. JNU202509RB021) and were performed in strict accordance with the ethical principles of the 1975 Declaration of Helsinki.

Mice

Ghr$^{f/f}$, *L-Ghr*$^{-/-}$, and *F/L-Ghr*$^{-/-}$ mice were generated as previously described [35,36]. *L-Ghr*$^{-/-}$&*Cfd*$^{-/-}$ mice were obtained from *L-Ghr*$^{-/-}$ crossed with *Cfd*$^{-/-}$ mice (Cyagen Biosciences, #KOAIP240329HZ2). All mice were housed in a specific pathogen-free (SPF) animal facility under standard laboratory conditions: constant room temperature (24–26°C), relative humidity of 40%–70%, and a 12h light/dark cycle with free access to standard chow diet (Xietong Shengwu, #XTI01WC-009) and sterile drinking water. All animal experiments were approved by the Institutional Animal Care and Use Committee of Jiangnan University and conducted in accordance with ethical guidelines for animal research (JN.NO20260914C120181[488]).

Ad libitum-fed 12-week-old *Ghr*$^{f/f}$, *L-Ghr*$^{-/-}$, *F/L-Ghr*$^{-/-}$, and *L-Ghr*$^{-/-}$& *Cfd*$^{-/-}$ mice were used in study. To achieve adipose-specific *Cfd* knockdown in *L-Ghr*$^{-/-}$ mice, 6-8 weeks old *L-Ghr*$^{-/-}$ mice were injected with 2×10^{11} vector genomes of AAV8-FABP4-eGFP-miR30-*Cfd* shRNA (Genomeditech, Shanghai, China) into the abdominal and subcutaneous adipose depots and maintained with for 5 weeks. To achieve liver-specific *Insr* knockdown in *L-Ghr*$^{-/-}$ mice, mice aged 6–8 weeks received an i.v. injection of 2×10^{11} vector genome of AAV8-TBG-eGFP-miR30-*Insr*-shRNA (Genomeditech, Shanghai, China) and were maintained for 5 weeks. For the diet-induced obesity (DIO) model, 8-week-old male *Cfd*$^{-/-}$ mice and WT controls were fed

60% HFD (TrophicDiet, #TP23300) for 6 weeks.

For pharmacological interventions experiments, 8-week-old male *L-Ghr*$^{-/-}$ mice were used. To inhibit CFD, mice received FD-IN-1 (MedChemExpress, #HY-128570) at 2.5 mg/kg or vehicle (10% DMSO in corn oil) via both in situ injection into inguinal and interscapular adipose tissues and intraperitoneal (i.p.) injection, three times per week for 2 weeks. To inhibit EVs secretion, mice were administered GW4869 (Ambeed, #A213331) at 2 mg/kg or vehicle (10% DMSO in saline) by i.p. injection three times per week for 2 weeks. To inhibit STAT5 signaling, mice received STAT5-IN-1 (MedChemExpress, #HY-101853) at 10 mg/kg or vehicle (10% DMSO in saline) via both in situ injection into adipose tissues and i.p. injection, three times per week for 2 weeks.

All mice were euthanized after a 6-h fast. Plasma and tissue samples were collected and stored at −80°C until further analyses.

Cell lines

HepG2 (Pricella, #CL-0103), Hepa1-6 (Pricella, #CL-0105), and HEK293T cells (ATCC, #CRL-1573) were cultured in high-glucose DMEM (Thermo Fisher Scientific, #C11995500BT) supplemented with 10% fetal bovine serum (FBS; ExCell, #FSD500) and 1% Pen-Strep (Biosharp, #BL505A). 3T3-L1 cells (Pricella, #CL-0006) were maintained in DMEM supplemented with 5% FBS and 1% Pen-Strep. Beta-TC-6 cells (Pricella, #CL-0322) were cultured in DMEM containing 20% FBS and 1% Pen-Strep. MIN6 cells (a gift from Dr. Zhuo-xian Meng) were cultured in DMEM supplemented with 10% FBS, 1% Pen-Strep, and 55μM β-mercaptoethanol (Sigma, #M6250). Stromal vascular fraction (SVF) cells were isolated from mouse inguinal white adipose tissue (iWAT) by collagenase digestion followed by cell straining and cultured in DMEM/F-12 (Thermo Fisher Scientific, #11320033) supplemented with 10% FBS and 1% Pen-Strep. 1.1B4 cells (MeisenCTCC, #CTCC-007-0127) were cultured in RPMI-1640 (Thermo Fisher Scientific, #11875500) supplemented with 10% FBS and 1% Pen-Strep. All cells were maintained at 37 °C in a humidified incubator with 5% CO_2.

Liver triglyceride measurements

Liver lipid extraction was performed as previously described [35]. Briefly, mice were euthanized by cervical dislocation, and the abdomen was immediately opened. The liver was rapidly harvested and freeze-clamped in situ. A frozen liver sample (100–150 mg) was homogenized in 4 mL of chloroform–methanol (2:1, v/v) using a D-130 rotary homogenizer (Wiggens, Germany). Subsequently, 0.8 mL of saline was added, and the mixture was vigorously vortexed. After centrifugation at 3,000 × g for 20 min, the lower organic phase was collected and transferred to a 5-mL volumetric flask. The final volume was adjusted to 5 mL with chloroform (Hushi, #10006818). Total triglyceride levels were measured using the assay kit (Jiancheng, #A110-1-1) according to the manufacturer's instructions.

Histological analysis

Paraffin-embedded liver sections were stained with hematoxylin and eosin (H&E;

Jiancheng, #D005-1-3/#D019-1-3) to assess hepatic steatosis. Paraffin-embedded pancreatic tissues were sectioned and stained with H&E to evaluate islet architecture, cellular distribution, and islet number and density. Hepatic lipid droplet accumulation was visualized by Oil Red O staining (Servicebio, #G1015) of frozen liver sections embedded in optimal cutting temperature (OCT) compound. Liver fibrosis was assessed by Sirius Red staining (Solarbio, #G1472). Liver and pancreas histology was examined and imaged using a Pannoramic MIDI digital slide scanner (3DHISTECH, Budapest, Hungary). For each mouse, at least three nonconsecutive tissue sections were examined.

Assays for plasma hormones, triglyceride, FFAs, ALT and AST

Mice were anesthetized with isoflurane, after which blood was drawn from the retro-orbital sinus and placed in EDTA-coated tubes. Plasma was obtained by centrifugation, and aliquots were stored at -80°C. Human plasma was obtained as described in above. Levels of hormones in plasma were determined with the following assay kits: mouse GH (Elabscience Biotechnology, #E-EL-M0060), mouse insulin (Crystal Chem, #90082), mouse C3a (Bio-Techne, #NBP2-70037), human insulin (Crystal Chem, #90095). Levels of triglyceride (Jiancheng, #A110-1-1), FFAs (Jiancheng, #A042-2-1), ALT (Jiancheng, #C009-2-1), and AST (Jiancheng, #C010-2-1) were measured using the indicated kits according to the manufacturers' protocols.

CFD ELISA assay

CFD levels were measured using an enzyme-linked immunosorbent assay (ELISA). The coating buffer was prepared by dissolving 3.03 g Na_2CO_3 and 6.0 g $NaHCO_3$ in 1 L of ddH_2O and adjusting the pH to 9.45. The blocking solution consisted of 1% BSA in PBS, and PBS was used as the wash buffer. Recombinant CFD peptide standards (0–100 ng/mL) were serially diluted in coating buffer. Mouse plasma, human plasma, plasma-derived EVs, and milk-derived EVs loaded with CFD were diluted 10-fold, 50-fold, 50-fold, and 50-fold, respectively. Aliquots (50 μL) of the diluted samples and standards were added to a 96-well plate, which was sealed and incubated overnight at 4 °C. After incubation, the coating solution was discarded, and the wells were washed three times with 200 μL PBS and blotted dry. Blocking solution was then added, and the plate was incubated for 2-h at room temperature. The wells were subsequently incubated with anti-CFD primary antibody (Invitrogen, #MA5-29686; 1:5,000 dilution) for 2-h, followed by four washes with PBS. A secondary antibody (Proteintech, #SA00001-2; 1:1,000) diluted in blocking solution was then added and incubated for 2-h. The wells were washed four times with PBS before the addition of tetramethylbenzidine (TMB) substrate (Yeasen, #36602ES60). After incubation for 15 min, the reaction was stopped by adding 2 M sulfuric acid (Hushi, #10021618), and absorbance was immediately measured at 450 nm.

Lipidomics analysis

Untargeted lipidomics of plasma samples was performed by an ACQUITY UPLC system (Waters) coupled with a tripleTOTM 5600 plus mass spectrometer (AB SCIEX).

Briefly, lyophilized samples were reconstituted in chloroform/methanol (2:1, v/v) and diluted threefold in ACN/IPA/H_2O (65:30:5, v/v/v) containing 5 mM ammonium acetate, and UPLC-MS/MS analysis was carried out by Metware Biotechnology Co., Ltd.

RNA isolation and real-time quantitative PCR

Total RNA was extracted using TRIzol reagent (Vazyme, #R401-01). cDNA was synthesized from 2μg total RNA using Hifair® III 1st Strand cDNA Synthesis SuperMix (Yeasen, #11141). The cDNAs were amplified by real-time PCR (qPCR) using Hieff qPCR SYBR Green Master Mix (Yeasen, #11201ES08). Relative gene expression levels were normalized to 36b4 and calculated using the $2^{-\Delta\Delta Ct}$ method. The primer sequences used for qPCR are listed in **Table S1**.

RNA-seq

RNA-seq analysis was performing following standard procedures in Metware Biotechnology Co., Ltd. (Wuhan, China). Total RNA was isolated from mouse liver tissues. RNA integrity numbers were determined using a Qsep400 high-throughput biofragment analyzer to ensure sample quality met the requirements for library construction. Fragmented mRNAs were used for reverse transcription and second-strand cDNA synthesis. Subsequently, adenine tailing and adaptor ligation were performed to prepare cDNAs for PCR amplification and double-stranded DNA library construction. The final library was amplified with phi29 to generate DNA nanoballs (DNBs), each containing more than 300 copies of a single molecule. The DNBs were loaded onto a sequencing chip and sequenced on the MGI sequencing platform. mRNA expression levels were calculated as FPKM. Differential expression analysis was performed using DESeq2 (v1.38.3), with an adjusted p-value (padj) < 0.05 and $|\log_2 FC| > 1$ as the cutoff. Volcano plots were generated using ggplot2 (v3.5.1). Venn diagrams were created using VennDiagram (v1.6.20). Heatmaps were generated using pheatmap (v1.0.12). Gene set enrichment analysis (GSEA) was performed using the R package ClusterProfiler (v4.6.0). The RNA-seq data have been deposited in the NCBI Gene Expression Omnibus under accession number: GSE325981.

Protein chip

A Proteome Profiler Mouse XL Cytokine Array (R&D Systems, #ARY028) was used to measure the relative levels of cytokines in mouse plasma samples. This semi-quantitative antibody array is based on the membrane-based sandwich immunoassay principle, and the assay was performed according to the manufacturer's instructions. Mouse plasma samples were incubated with biotinylated detection antibodies, and the resulting complexes were captured by antibodies pre-spotted on nitrocellulose membranes. After washing, streptavidin-HRP was added, followed by chemiluminescent detection. Signal intensities were quantified using Quick Spots software.

Plasma protein extraction and coomassie staining

Plasma samples were collected from mice and subjected to albumin depletion using an Immunodepletion Resin (R&D Systems, #MIDR002-040). The samples were then mixed with 5×protein loading buffer (Yeasen, #20315ES20), denatured by boiling, and then subjected to SDS-PAGE, followed by Coomassie Brilliant Blue staining (Beyotime, #P0017) for protein detection.

Metabolic cage measurement

Mice were individually acclimated in the CLAMS-16MR system (Columbus Instruments, USA) for 5 days, followed by continuous monitoring of metabolic parameters for 6 days using a pre-calibrated system. Oxygen consumption (VO_2) and carbon dioxide production (VCO_2) were continuously recorded to calculate the respiratory quotient ($RQ = VCO_2/VO_2$). Food intake was also continuously monitored. Throughout the measurement period, ambient conditions were kept constant, and mice had ad libitum access to food and water.

GTT and ITT

For GTT, 12-week-old male mice were fasted overnight (~16 h) with free access to sterile water. A 20% (w/v) glucose solution (Beyotime, #ST491) prepared in sterile physiological saline was administered i.p. at 2 g/kg body weight. Blood glucose levels were measured in tail-snip blood samples before injection and at 15, 30, 60, and 90 min after injection. For ITT, 12-week-old male mice were fasted for 6 h with free access to sterile water. Freshly prepared insulin solution (Yuanye, #S31559) was injected i.p. at 1 U/kg body weight, blood glucose levels were measured at pre-injection, 15, 30, 60, and 90 min after injection. The area under the blood glucose–time curve (AUC) was calculated using the trapezoidal method.

Immunohistochemistry staining

Formalin-fixed, paraffin-embedded (FFPE) sections of mouse eWAT, iWAT, and BAT were incubated overnight at 4 °C with an anti-CFD antibody (Invitrogen, #MA5-29686; 1:200) and visualized using a DAB kit (Servicebio, #G1212). Pancreatic sections were incubated overnight at 4 °C with an anti-insulin antibody (Invitrogen, #PA5-120784; 1:100) and visualized using the same DAB kit.

Immunofluorescence staining

Cells grown on coverslips were fixed with 4% paraformaldehyde for 15 min at room temperature, permeabilized with 0.1% Triton X-100 for 10 min, and blocked with 5% BSA in PBS for 20 min at room temperature. After overnight incubation at 4 °C with primary antibodies (anti-PPARγ rabbit mAb: CST, #2435S, 1:200; anti-STAT5B mouse mAb: Proteintech, #66427-1-Ig, 1:200), cells were incubated with fluorescent secondary antibodies (CoraLite 594-conjugated goat anti-mouse IgG (H+L): Proteintech, #SA00013-3, 1:500; CoraLite 488-conjugated goat anti-rabbit IgG (H+L): Proteintech, #SA00013-2, 1:500) for 1 h at room temperature in the dark. Nuclei were stained with DAPI (Beyotime, #C1006) for 3 min, and coverslips were mounted with anti-fade mounting medium. For exogenous protein expression, cells were

cotransfected with Flag-*Pparγ* and HA-*Stat5b* then subjected to GH stimulation. Immunofluorescence assay was performed as described above; anti-Flag (Proteintech, #66008-4-Ig, 1:500) and anti-HA (Proteintech, #81290-1-RR, 1:500) primary antibodies were used to detect the Flag- and HA-tagged proteins, respectively. For pancreatic tissue sections, deparaffinization, rehydration, and antigen retrieval (Beyotime, #P0083) were performed. Sections were incubated overnight at 4 °C with anti-insulin rabbit pAb (Invitrogen, #PA5-120784, 1:100) and anti-glucagon mouse mAb (Proteintech, #67286-1-Ig, 1:200), followed by the same blocking and secondary antibody steps as described above. Images were captured using an Axio Vert A1 inverted fluorescence microscope (Zeiss, Germany).

Adipogenic differentiation of primary mouse adipose SVF cells and 3T3-L1 cells

Primary adipose SVF cells were isolated as described by Tang et al. [37]. Briefly, mice were sacrificed, and inguinal WAT was dissected, minced, and digested by collagenase type I (Thermo Fisher Scientific, #17018029) in a shaking water bath for 1 h at 37 °C. The resulting cell suspension was filtered through a cell strainer, centrifuged, resuspended, and plated. All isolation steps were performed under strict sterile conditions to ensure cell viability and purity. Differentiation of SVF cells into adipocytes was induced in DMEM/F12 (Thermo Fisher Scientific, #11320033) supplemented with 10% FBS, 1% Pen/Strep, 0.5 mM IBMX (Aladdin, #I106812), 1 μM dexamethasone (Sigma, #D4902), 5 μg/mL insulin (Yuanye, #S31559), and 1 μM rosiglitazone (MedChemExpress, #HY-17386) for 48 h. Cells were then maintained in medium containing 5 μg/mL insulin, with the medium refreshed every 2 days. Adipogenic differentiation of 3T3-L1 cells was induced with the same MDI cocktail in high-glucose DMEM supplemented with 10% FBS and 1% penicillin–streptomycin for 48 h, followed by maintenance in insulin-containing (5 μg/mL) medium refreshed every 2 days.

Plasmid construction

Full-length cDNAs of mouse *Stat5a* and *Stat5b* were amplified from SVF cells. The *Stat5b* cDNA was cloned into the pcDNA3.3 vector with an HA tag inserted at the N-terminus, and the *Stat5a* cDNA was cloned into the same vector with an HA tag inserted at the C-terminus. Different fragments of the *Cfd* promoter were cloned into the pGL3-Basic vector. sgRNA targeting *Ghr* was cloned into PX459 vector. Primer sequences used for plasmid construction are listed in **Table S2**.

siRNA-mediated gene silencing

For siRNA transfection, SVF or 3T3-L1 cells at 50%–60% confluence were incubated with siRNA targeting STAT5A, STAT5B, or a scramble control using Lipofectamine 2000 Transfection Reagent (Invitrogen, #11668019) according to the manufacturer's instructions. Briefly, the appropriate siRNA was diluted in Opti-MEM (Thermo Fisher Scientific, #31085-70) and combined with Lipofectamine 2000 to form the transfection complex. After incubation for 15 min at room temperature, the transfection mixture was added to the culture medium, and the cells were differentiated for 2 days to allow

optimal gene knockdown before subsequent assays. The siRNA sequences for targeted gene knockdown were provided in **Table S3**.

shRNA lentivirus generation

shRNA sequences listed in **Table S4** were cloned into the pLKO.1 vector. HEK293T cells were seeded at 1×10^7 cells per 100-mm dish on day 0. On day 2, 5 μg of knockdown vector, 3 μg of psPAX2 packaging plasmid, and 2 μg of pMD2.G envelope plasmid were co-transfected using polyethylenimine (MedChemExpress, #HY-W250110E) according to the manufacturer's protocol. Culture media were harvested at 48h post-transfection, filtered through 0.45μm filter membrane, centrifugated at 4000rpm for 10min at 4℃ to pellet cell debris, then used a Universal Virus Concentration Kit (Beyotime, #C2901M-1) to concentrate the viral titer and stored at -80℃ until use.

CUT & Tag and analysis

CUT&Tag assays were performed in 3T3-L1 cells using the Hyperactive Universal CUT&Tag Assay Kit (Vazyme, #TD904-01). Briefly, cells were trypsinized, counted, and washed with PBS. A total of 1×10^5 cells were resuspended in 100 μL pre-cooled NE Buffer, incubated on ice for 10 min to isolate nuclei, and centrifuged at 600 × g for 5 min at room temperature. After discarding the supernatant, the nuclear pellets were resuspended in 100 μL Wash Buffer. ConA Beads Pro were activated with Binding Buffer, and 100 μL nuclei were incubated with 10 μL activated beads for 10 min at room temperature. Then, 50 μL pre-cooled Antibody Buffer containing 5% digitonin was added to resuspend the complex, followed by overnight incubation at 4 °C with ChIP-grade primary antibodies (anti-PPARγ: #2435S, 1:100; anti-STAT5: #94205S, 1:100; normal IgG: Proteintech, #B900620, 1:100). After washing with 200 μL Dig-wash Buffer, the complex was incubated with 50 μL diluted secondary antibody (anti-rabbit IgG for IP: Vazyme, #RA1008-01, 1:100) for 60 min at room temperature and washed again. Next, 100 μL diluted pA/G-Tnp Pro (final concentration 0.04 μM) was added for 1 h at room temperature, followed by washing with Dig-300 Buffer. Fragmentation was performed with 50 μL diluted TTBL in Dig-300 Buffer at 37 °C for 60 min. Then, 2 μL 10% SDS and 1 μL DNA Spike-in were added, and the mixture was incubated at 55 °C for 10 min. After magnetic separation, the supernatant was collected and mixed with 50 μL activated DNA Extract Beads Pro for DNA extraction. The DNA–bead complex was resuspended in 15 μL ddH_2O and used for library amplification with 25 μL 2× CAM and index primers (N502/N701) for 20 cycles. PCR products were purified with 100 μL VAHTS DNA Clean Beads according to the manufacturer's instructions, eluted in 22 μL ddH_2O, and 20 μL supernatant was transferred to a new tube and stored at −20 °C. Library concentration was measured using Qubit 3.0 (Thermo Fisher Scientific, USA), and fragment integrity was assessed using a Bioanalyzer 2100 (Agilent, CA, USA). PE150 sequencing was performed on an Illumina NovaSeq XP according to standard protocols.

Raw sequencing reads were processed with fastp for quality control to remove adapter sequences, low-quality bases, and short fragments, generating clean reads.

Clean reads were aligned to the mouse reference genome (GRCm39) using bowtie2. Low-quality alignments were filtered with samtools, and PCR duplicates were removed with sambamba. Peak calling was performed using MACS2, and significant peaks were defined as FDR < 0.05. Peaks were annotated using ChIPseeker. Differential binding analysis was performed on the VZ-Biocloud Platform (https://vazyme-biocloud.vazyme.com:5174/).

Dual-luciferase reporter assay

3T3-L1 cells were co-transfected with a *Cfd* promoter luciferase reporter and a Renilla luciferase reporter, followed by overexpression of PPARγ, STAT5A, or STAT5B; knockdown of *Stat5a* or *Stat5b*; or treatment with T0070907 (MedChemExpress, #HY-13202), pioglitazone (MedChemExpress, #HY-13956), or GH (MedChemExpress, #HY-P70261), as indicated. Luciferase activity was measured using a microplate reader (Agilent, USA) and a dual-luciferase detection kit (Yeasen, #11402ES80). Firefly luciferase activity was normalized to Renilla luciferase activity (Firefly/Renilla ratio).

ChIP & Re-ChIP

These assays were performed with modifications of the procedure described by Reid et al. [38]. For ChIP, cells were cross-linked with 1% formaldehyde (Titan, #G60216A) for 10 min at room temperature, and the reaction was quenched by adding glycine to 0.125 M for 5 min. Cells were lysed in pre-chilled lysis buffer (150 mM NaCl, 10 mM EDTA, 50 mM Tris-HCl, pH 8.0, 0.1% Triton X-100, 0.1% SDS) supplemented with protease inhibitors. Chromatin was sheared to approximately 500 bp using a sonicator (30 s on/60 s off for 15 min at 50%), and samples were centrifuged at 14,000 rpm for 10 min at 4 °C. The supernatant was collected, aliquoted, and stored at −80 °C; a 20 µL aliquot was reserved as input. For immunoprecipitation, 200 µg of sheared chromatin was diluted to 0.5 mL with dilution buffer (2 mM EDTA, 0.1% Triton X-100, 150 mM NaCl, 20 mM Tris-HCl, pH 8.0, 0.01% SDS) and incubated overnight at 4 °C with rotation with 2 µg of anti-IgG (Proteintech, #30000-0-AP), anti-PPARγ (CST, #2435S), or anti-STAT5B (Zenbio, #R27320). The next day, 20 µL of protein A/G magnetic beads (Yeasen, #36417ES) were added and incubated for 60 min at 4 °C. Beads were washed sequentially with low-salt, high-salt, LiCl, and TE buffers (5 min each at 4 °C with rotation). Immune complexes were eluted with 100 µL elution buffer (0.1 M $NaHCO_3$, 1% SDS) at 65 °C for 30 min, and cross-links were reversed overnight at 65 °C. DNA was purified using a DNA Purification Kit (Beyotime, #D0033) and analyzed by qPCR with primers listed in **Table S5**.

For Re-ChIP, cells were cross-linked with 1% formaldehyde (Titan, #G60216A) for 10 min at room temperature, and the reaction was stopped with glycine solution (Hushi, #62011519). Chromatin was sonicated in lysis buffer containing 1× protease inhibitor cocktail. After centrifugation, 20 µL of the supernatant was retained as input, and 500 µg of chromatin was incubated overnight at 4 °C with rotation with 2 µg of anti-STAT5B rabbit mAb. The next day, 20 µL of protein A/G magnetic beads were added and incubated for 60 min at 4 °C. Beads were washed sequentially with low-salt, high-salt, LiCl, and TE buffers (5 min each at 4 °C with rotation). Complexes were eluted

with 100 μL Re-ChIP buffer (0.5 mM DTT, 1% Triton X-100, 2 mM EDTA, 150 mM NaCl, 20 mM Tris-HCl, pH 8.1) at 37 °C for 30 min. The eluate was then incubated overnight at 4 °C with rotation with 2 μg of anti-IgG or anti-PPARγ rabbit mAb. The next day, 20 μL of protein A/G magnetic beads were added and incubated for 60 min at 4 °C. Beads were washed and complexes were eluted as described above for ChIP. Cross-links were reversed overnight at 65 °C, and DNA was purified for qPCR.

Protein extraction and immunoblotting

RIPA buffer (50 mM Tris-HCl, pH 8.0; 150 mM NaCl; 0.5% sodium deoxycholate; 1% Triton X-100; and 10% glycerol), supplemented with protease inhibitor cocktail (Thermo Fisher Scientific, #A32955) and phosphatase inhibitor mixture (NCM, #P003), was used to lyse tissues or cells on ice for 30–45 min. Protein concentration was determined using a Pierce BCA Protein Assay Kit (Thermo Fisher Scientific, #23225). Plasma samples were pretreated with Immunodepletion Resin (R&D Systems, #MIDR002-040). The extracts were mixed with SDS loading buffer, and boiled at 100 °C for 5 min and then subjected to SDS-PAGE, transferred to nitrocellulose filters, followed by immunoblotting with the following primary antibodies: ACC1 (Proteintech, #67373-1-Ig; 1:5,000), FAS (Proteintech, #66591-1-Ig; 1:5,000), SCD1 (CST, #2794S; 1:1,000), SREBP1 (Thermo Fisher Scientific, #MA5-11685; 1:2,000), GAPDH (Proteintech, #60004-1-Ig; 1:10,000), CFD (Invitrogen, #MA5-29686; 1:2,000), HSP90 (Proteintech, #13171-1-AP; 1:10,000), insulin receptor α (CST, #74118S; 1:1,000), insulin receptor β (CST, #23413S; 1:1,000), ALIX (Proteintech, #67715-1-Ig; 1:2,000), PPARγ (CST, #2435S; 1:1,000), STAT5 (CST, #94205S; 1:2,000), phospho-STAT5 (Tyr694) (C11C5) (CST, #9359S; 1:1,000), STAT5A (Proteintech, #51074-2-AP; 1:1,000), STAT5B (Zenbio, #R27320; 1:1,000), Calnexin (Proteintech, #66903-1-Ig; 1:1,000), CD9 (Proteintech, #82105-1-RR; 1:1,000), Lamin A/C (Proteintech, #10298-1-AP; 1:5,000), HA-tag (Proteintech, #81290-1-RR; 1:10,000), Flag-tag (Proteintech, #66008-4-Ig; 1:10,000), TSG101 (Proteintech, #67381-1-Ig; 1:1,000), and GHR (Abcam, #ab202964; 1:1,000).

Immunoprecipitation (IP)

Cells were lysed with RIPA buffer and homogenized. A total of 300 μg of homogenate protein was incubated with anti-FLAG magnetic beads (MedChemExpress, #HY-K0207) or anti-HA magnetic beads (Yeasen, #20566ES03) at 4 °C for 12–16 h. The beads were washed three times with cold TBST buffer, and bound proteins were eluted with 50 μL SDS loading buffer and analyzed by immunoblotting.

Construction of stable cell lines

A plasmid encoding an sgRNA targeting *Ghr* was transfected into 3T3-L1 cells. At 48 h post-transfection, the medium was replaced with fresh medium containing puromycin (1–10 μg/mL), and cells were selected for one week. Surviving cells were trypsinized and re-plated into 96-well plates for single-cell isolation and clonal expansion. Finally, RT-qPCR or/and immunoblotting were used to verify gene knockout efficiency.

Nuclear-cytoplasmic fractionation

Cytoplasmic and nuclear proteins were extracted using a Nuclear and Cytoplasmic Protein Extraction Kit (Thermo Fisher Scientific, #78833) for immunoblot analysis of protein subcellular localization.

Extracellular vesicle (EV) purification

For plasma EV purification, frozen mouse or human plasma was thawed on ice, pooled within each group, and then diluted to 2 mL with ice-cold particle-free saline. The diluted plasma was centrifuged at 2,000 × g for 10 min at 4 °C to remove large particles, and the supernatant was centrifuged at 10,000 × g for 45 min at 4 °C to collect crude EVs. The resulting supernatant was transferred to polypropylene tubes and ultracentrifuged at 100,000 × g for 2 h at 4 °C with maximum acceleration and deceleration set to 0 to pellet refined EVs. The refined EV-containing pellet was resuspended in 10 mL ice-cold particle-free PBS, washed by ultracentrifugation at 100,000 × g for 2 h at 4 °C, and finally resuspended in 30–100 μL ice-cold particle-free PBS. Particle-free PBS (0.22 μm filtered) was used throughout to minimize interference, and EV quality was performed as described below.

Loading of CFD recombination protein into milk exosomes

Fresh bovine milk was stored at 4 °C until use. Milk was subjected to sequential differential ultracentrifugation, and the supernatant was collected. The supernatant was acidified with acetic acid to pH 4.6 to remove casein. The casein-depleted supernatant was then passed through a 0.22 μm membrane filter, and the filtrate was further ultracentrifuged at 140,000 × g for 90 min to isolate milk-derived exosomes, which were resuspended in PBS and stored at −80 °C until use. An appropriate amount of recombinant CFD protein (MedChemExpress, #HY-P7876) was resuspended in PBS and loaded into milk exosomes by electroporation using an electroporator (Eppendorf, Germany) at 300 V for four cycles to transiently permeabilize the membrane and facilitate protein encapsulation. The suspension was then incubated at room temperature for 10 min to allow membrane recovery. Subsequently, the sample was ultracentrifuged at 140,000 × g for 60 min to remove unincorporated protein remaining in the supernatant. The collected CFD-loaded exosomes were resuspended and stored at −80 °C.

Nanoparticle tracking analysis (NTA)

Particle concentration (particles mL^{-1}) and size distribution of EVs were measured in real time using a NanoSight NS300 instrument (Malvern Panalytical, UK) equipped with an sCMOS camera. Before analysis, samples were filtered through a 0.45 μm membrane and introduced under a controlled, constant flow. Temperature was not specifically controlled during recording. The camera level and detection threshold were set to 11 and 25, respectively. For each sample, five consecutive 60 s videos were recorded and analyzed using NTA 3.4 Build software. The modal size distribution was obtained by averaging the replicate histograms.

Transmission electron microscopy (TEM)
EV morphology was examined by TEM using a JEM-2100PLUS instrument (JEOL, Japan) operated at 100 kV. Before imaging, samples were filtered through a 0.45 μm membrane, and then negatively stained with uranyl acetate on Formvar/carbon-coated copper grids at room temperature.

Dynamic light scattering (DLS)
The hydrodynamic size distribution of milk control EVs and CFD-EVs was measured using a Zetasizer Nano system (Malvern Panalytical, UK) with DTS0012 disposable cuvettes (Brand, Germany). Measurements were performed in triplicate, using protein as the sample material and water as the dispersant.

Mouse primary islet isolation
Mouse islets were isolated from the pancreas by intraductal digestion with collagenase type V (1 mg/mL; Sigma-Aldrich, #C9263) and purified by density gradient centrifugation using Histopaque 1119 (Sigma-Aldrich, #11191), as described by Meng et al. [21,39]. Purified islets were hand-picked under a stereomicroscope and incubated in RPMI-1640 medium for subsequent assays.

GSIS assay
Primary mouse islets (20 islet equivalents, IEQ), β-TC6 cells (5×10^4 cells/well), or MIN6 cells (1×10^5 cells/well) were preincubated for 30 min in glucose-free Krebs buffer and then incubated in Krebs buffer containing 2.8- or 16.8- mM glucose for 45 min. Supernatants were collected after static incubation for insulin measurement. Cells were lysed for total protein quantification by BCA assay (Thermo Fisher Scientific, #23225) or for genomic DNA extraction using the MolPure Cell/Tissue DNA Kit (Yeasen, #18700ES50). Insulin secretion under each condition was quantified using an insulin assay kit (Crystal Chem, #90082) according to the manufacturer's instructions and normalized to total protein or DNA content.

Measurement of intracellular ATP/ADP ratio
Primary mouse islets (20 IEQ), β-TC6 cells (5×10^4 cells/well) or Min6 cells (1×10^5 cells/well) were incubated in Krebs buffer containing 2.8- or 16.8-mM glucose for 45 min. For EV treatment, islets were incubated in Krebs buffer containing 16.8 mM glucose. ATP and ADP levels were quantified using an ATP Assay Kit (MedChemExpress, #HY-K0314) and an Amplex Red ADP Assay Kit (Beyotime, #S0307S), respectively, and the intracellular ATP/ADP ratio was calculated.

Imaging and measurement of intracellular calcium
Primary murine islets (50 IEQ) cultured overnight after isolation were washed twice with Krebs buffer and incubated in Krebs buffer containing 5 μM Fluo-4 AM (Thermo Fisher Scientific, #F14201), 0.04 % Pluronic F127 (Yeasen, #60318ES60), and 2.8- or 16.8-mM glucose for 25 min. Islets were then washed with Krebs buffer containing 2.8- or 16.8-mM glucose, placed in a 35-mm glass-bottom dish (Biosharp Biotechnology,

China), and incubated for an additional 5 min. For EV treatment, islets were loaded and washed with Krebs buffer containing 16.8 mM glucose. Islets were imaged in a humidified 37 °C cell culture chamber with 5% CO_2 using a Dragonfly 202 confocal microscope (Andor, UK). Images were acquired continuously at 50-ms intervals until the fluorescence signal reached a plateau; total fluorescence intensity was then measured at 488 nm. Dynamic changes in fluorescence intensity were analyzed using ImageJ. For Min6 cells assay, 1×10^5 cells were pre-plated in 35-mm glass-bottom confocal dishes and subjected to the same protocol as described above for imaging and measurement of intracellular calcium.

Measurement of oxygen consumption rate (OCR)

OCR were measured using the Seahorse XF Pro (Agilent, USA) in conjunction with Seahorse XF Cell Mito Stress Test Kit (Agilent, #103015-100), following the manufacturer's instructions. Briefly, Min6 cells were seeded at 5×10^4 cells per well in XF Pro cell culture microplates in 100 μL DMEM, with at least four cell-free wells for background correction, and allowed to attach overnight at 37 °C with 5% CO_2. The XF Pro sensor cartridge was hydrated overnight at 37 °C in a non-CO_2 incubator with 180 μL XF Calibrant per well. On the day of assay, the medium was gently removed, and monolayers were washed once with pre-warmed XF assay medium before 180 μL of the same medium was added to each well. Cells were then treated with CFD-loaded EVs or control milk EVs and incubated in a non-CO_2 incubator for 45–60 min. Compounds were loaded into the sensor cartridge ports to give final concentrations of 16.8 mM glucose, 1.5 μM oligomycin, 2 μM FCCP, and 500 nM of rotenone/ antimycin A. Basal OCR was recorded before sequential injections, and OCR after each injection was used to calculate basal respiration, ATP production, and maximal respiration. OCR values were normalized to total protein content per well.

Pancreatic ductal infusion of EVs

Pancreatic ductal infusion was performed as previously described by Xaio et al. [40]. Male *Cfd* $^{-/-}$ mice (8-week-old) were anesthetized with 2–2.5% isoflurane and placed on a 37 °C sterile heating pad. The lower chest and abdomen were shaved and disinfected with 75% ethanol (Titan, #G73537O). A 1.5-cm midline laparotomy was performed in the upper abdomen to expose the choledochopancreatic duct and the sphincter of Oddi. A vascular clamp was placed on the common bile duct proximal to the duodenum to prevent hepatic perfusion, and a 30-gauge catheter was inserted through a small duodenal puncture (1–2 mm from the ampulla) into the sphincter of Oddi and secured to prevent leakage. A 50 μL solution (4.72×10^7 EVs, 200 μg/mL CFD; 10 ng total) was infused at 6 μL/min using an infusion pump (Leadfluid, China) connected to the catheter. After infusion, the catheter was withdrawn, and the duodenal puncture and abdominal incision were closed with 6-0 sutures. Mice were kept on the heating blanket for recovery after the procedure.

Statistical analysis

Statistical tests were applied with the sample sizes listed in the figure legends. All data

were analyzed using GraphPad Prism 9.0. Statistical comparisons between two groups were made by the unpaired Student's test, and for comparison multiple groups were performed using one-way or two-way ANOVA followed by Tukey's or Bonferroni's post hoc test, as indicated in the figure legends. Differences were considered statistically significant at $p < 0.05$. The data that support the findings of this study are available from the corresponding authors upon reasonable request.

Data availability

All data generated or analyzed during this study are included in this article and its supplementary information files. The RNA-seq data have been deposited in the NCBI Gene Expression Omnibus under accession number: GSE325981. The data from lipidomic analysis were deposited to the OMIX (https://ngdc.cncb.ac.cn/omix/) with the dataset identifier OMIX023205. Source data are provided with this paper.

References

1. Younossi, Z.M., *et al.* The global epidemiology of nonalcoholic fatty liver disease (NAFLD) and nonalcoholic steatohepatitis (NASH): a systematic review. *Hepatology* **77**, 1335-1347 (2023).
2. Powell, E.E., Wong, V.W. & Rinella, M. Non-alcoholic fatty liver disease. *Lancet* **397**, 2212-2224 (2021).
3. Feng, G., *et al.* Recompensation in cirrhosis: unravelling the evolving natural history of nonalcoholic fatty liver disease. *Nat Rev Gastroenterol Hepatol* **21**, 46-56 (2024).
4. Samuel, V.T. & Shulman, G.I. Nonalcoholic Fatty Liver Disease as a Nexus of Metabolic and Hepatic Diseases. *Cell Metab* **27**, 22-41 (2018).
5. Lee, W.H., *et al.* The physiology of MASLD: molecular pathways between liver and adipose tissues. *Clin Sci (Lond)* **139**, 1015-1046 (2025).
6. Wetterau, J.R., *et al.* Absence of microsomal triglyceride transfer protein in individuals with abetalipoproteinemia. *Science* **258**, 999-1001 (1992).
7. Miquilena-Colina, M.E., *et al.* Hepatic fatty acid translocase CD36 upregulation is associated with insulin resistance, hyperinsulinaemia and increased steatosis in non-alcoholic steatohepatitis and chronic hepatitis C. *Gut* **60**, 1394-1402 (2011).
8. Sanders, F.W. & Griffin, J.L. De novo lipogenesis in the liver in health and disease: more than just a shunting yard for glucose. *Biol Rev Camb Philos Soc* **91**, 452-468 (2016).
9. Ma, I.L. & Stanley, T.L. Growth hormone and nonalcoholic fatty liver disease. *Immunometabolism (Cobham)* **5**, e00030 (2023).
10. Fan, Y., *et al.* Liver-specific deletion of the growth hormone receptor reveals essential role of growth hormone signaling in hepatic lipid metabolism. *J Biol Chem* **284**, 19937-19944 (2009).
11. List, E.O., *et al.* Liver-specific GH receptor gene-disrupted (LiGHRKO) mice have decreased endocrine IGF-I, increased local IGF-I, and altered body size, body composition, and adipokine profiles. *Endocrinology* **155**, 1793-1805 (2014).
12. Liu, Z., *et al.* Growth Hormone Control of Hepatic Lipid Metabolism. *Diabetes* **65**, 3598-

3609 (2016).
13. Ran, L., *et al.* Loss of Adipose Growth Hormone Receptor in Mice Enhances Local Fatty Acid Trapping and Impairs Brown Adipose Tissue Thermogenesis. *iScience* **16**, 106-121 (2019).
14. Xu, Y., *et al.* Complement activation in factor D-deficient mice. *Proc Natl Acad Sci U S A* **98**, 14577-14582 (2001).
15. Lo, J.C., *et al.* Adipsin is an adipokine that improves beta cell function in diabetes. *Cell* **158**, 41-53 (2014).
16. Gomez-Banoy, N., *et al.* Adipsin preserves beta cells in diabetic mice and associates with protection from type 2 diabetes in humans. *Nat Med* **25**, 1739-1747 (2019).
17. Aaron, N., *et al.* Adipsin promotes bone marrow adiposity by priming mesenchymal stem cells. *Elife* **10**(2021).
18. Guo, R., *et al.* Complement factor D is a drug target for metabolic-associated fatty liver disease. *Mol Immunol* **188**, 192-200 (2025).
19. Zhang, X., *et al.* Adipsin alleviates cardiac microvascular injury in diabetic cardiomyopathy through Csk-dependent signaling mechanism. *BMC Med* **21**, 197 (2023).
20. Liang, W., *et al.* Mitochondria are secreted in extracellular vesicles when lysosomal function is impaired. *Nat Commun* **14**, 5031 (2023).
21. Wang, R.R., *et al.* Dietary intervention preserves beta cell function in mice through CTCF-mediated transcriptional reprogramming. *J Exp Med* **219**(2022).
22. Karki, R.G., *et al.* Design, Synthesis, and Preclinical Characterization of Selective Factor D Inhibitors Targeting the Alternative Complement Pathway. *J Med Chem* **62**, 4656-4668 (2019).
23. Kong, Y., *et al.* Role of complement factor D in cardiovascular and metabolic diseases. *Front Immunol* **15**, 1453030 (2024).
24. Kulaj, K., *et al.* Adipocyte-derived extracellular vesicles increase insulin secretion through transport of insulinotropic protein cargo. *Nat Commun* **14**, 709 (2023).
25. Thery, C., *et al.* Minimal information for studies of extracellular vesicles 2018 (MISEV2018): a position statement of the International Society for Extracellular Vesicles and update of the MISEV2014 guidelines. *J Extracell Vesicles* **7**, 1535750 (2018).
26. Shu, C., *et al.* C3a-C3aR signaling promotes breast cancer lung metastasis via modulating carcinoma associated fibroblasts. *J Exp Clin Cancer Res* **39**, 11 (2020).
27. Wang, Y., Viscarra, J., Kim, S.J. & Sul, H.S. Transcriptional regulation of hepatic lipogenesis. *Nat Rev Mol Cell Biol* **16**, 678-689 (2015).
28. Njei, B., Ameyaw, P., Al-Ajlouni, Y., Njei, L.P. & Boateng, S. Diagnosis and Management of Lean Metabolic Dysfunction-Associated Steatotic Liver Disease (MASLD): A Systematic Review. *Cureus* **16**, e71451 (2024).
29. Danpanichkul, P., *et al.* Long-term outcomes and risk modifiers of metabolic dysfunction-associated steatotic liver disease between lean and non-lean populations. *Clin Mol Hepatol* **31**, 74-89 (2025).
30. Kong, T., *et al.* Association of nonalcoholic fatty liver disease and growth hormone deficiency: a systematic review and meta-analysis. *Endocr J* **70**, 959-967 (2023).
31. Takahashi, Y. Nonalcoholic fatty liver disease and adult growth hormone deficiency: An under-recognized association? *Best Pract Res Clin Endocrinol Metab* **37**, 101816 (2023).

32. Dichtel, L.E., *et al.* Growth Hormone Administration Improves Nonalcoholic Fatty Liver Disease in Overweight/Obesity: A Randomized Trial. *J Clin Endocrinol Metab* **108**, e1542-e1550 (2023).
33. Kim, J.K., Choi, C.S. & Youn, J.H. Acute effect of growth hormone to induce peripheral insulin resistance is independent of FFA and insulin levels in rats. *Am J Physiol* **277**, E742-749 (1999).
34. Nellemann, B., *et al.* Growth hormone-induced insulin resistance in human subjects involves reduced pyruvate dehydrogenase activity. *Acta Physiol (Oxf)* **210**, 392-402 (2014).
35. Fang, F., Shi, X., Brown, M.S., Goldstein, J.L. & Liang, G. Growth hormone acts on liver to stimulate autophagy, support glucose production, and preserve blood glucose in chronically starved mice. *Proc Natl Acad Sci U S A* **116**, 7449-7454 (2019).
36. Fang, F., Goldstein, J.L., Shi, X., Liang, G. & Brown, M.S. Unexpected role for IGF-1 in starvation: Maintenance of blood glucose. *Proc Natl Acad Sci U S A* **119**, e2208855119 (2022).
37. Tang, W., *et al.* White fat progenitor cells reside in the adipose vasculature. *Science* **322**, 583-586 (2008).
38. Reid, G., *et al.* Cyclic, proteasome-mediated turnover of unliganded and liganded ERalpha on responsive promoters is an integral feature of estrogen signaling. *Mol Cell* **11**, 695-707 (2003).
39. Meng, Z.X., *et al.* Activation of liver X receptors inhibits pancreatic islet beta cell proliferation through cell cycle arrest. *Diabetologia* **52**, 125-135 (2009).
40. Xiao, X., *et al.* Pancreatic cell tracing, lineage tagging and targeted genetic manipulations in multiple cell types using pancreatic ductal infusion of adeno-associated viral vectors and/or cell-tagging dyes. *Nat Protoc* **9**, 2719-2724 (2014).

Acknowledgments

We thank Drs. Li Qiang (Peking University), Lin-Zhang Huang (Fudan University), Tong-Jin Zhao (Fudan University), and Ying Liu (Jiangnan University) for providing plasmids. We are also grateful to Dr. Zhuo-Xian Meng (Zhejiang University) for providing cell lines and helping with primary islet isolation. This work was supported by grants from the National Natural Science Foundation of China (82470618), and Jiangsu Provincial Distinguished Professor Funding Program (1286010241231180, 1286010241250480).

Author contributions

P.W. and F.F. conceptualized the project and designed the experiments. P.W., J.C., and T.W. performed the experiments and analyzed the data. C.X. contributed to the collection of human liver specimens and subsequent staining of human liver slides. Y.W. contributed to primary islet isolation. Y.Z. contributed to RNA-seq analysis. K.W., F.G., L.W., G.D., R.Z., and C.L. contributed to cell culture and mouse sample collection. Tao Wan provided milk exosomes and assisted in constructing CFD-loaded EVs and

characterizing these EVs. Z.L. provided human plasma samples and liver slides and contributed to writing–review and editing. P.W. and F.F. wrote the manuscript. F.F. supervised the project.

Competing interests

The authors declare no competing interests.

Figure legends

Figure 1. Phenotypes among *Ghr*$^{f/f}$, *L-Ghr*$^{-/-}$, and *F/L-Ghr*$^{-/-}$ *mice*.
a Representative photograph of age-matched (12-week-old) male *Ghr*$^{f/f}$, *L-Ghr*$^{-/-}$, and *F/L-Ghr*$^{-/-}$ mice and their isolated livers. **b** Quantification of liver-to-body weight ratios across experimental groups. n=7/group. **c** Measurement of hepatic triglyceride (TG) content. n=7/group. **d** Histological staining of liver sections. Hematoxylin-eosin (H&E) staining (up), Oil-Red-O staining (middle), and was Picrosirius red (PSR) staining (bottom). n=7/group. Scale bar, 50 μm. **e** Plasma levels of alanine aminotransferase (ALT). **f** Plasma levels of aspartate aminotransferase (AST). n=7/group. **g** Quantification of total plasma triglycerides. n=7/group. **h** Plasma triglyceride lipidomic profiling stratified by acyl-chain length. n= 4/group. **i** Measurement of total plasma free fatty acids (FFA). n=7/group. **j** Chain-length-resolved profiling of plasma free fatty acids. n=4/group. **k** Average daily food intake across the three male genotypes. n=7/group. **l** Respiratory exchange ratio over 6 days in male mice of the three genotypes. Grey color indicates dark phase when light was off. Data are presented as means ± SD. n=4/group.
Data (b-c, e-k) are presented as individual values with the means. p values were determined by one-way ANOVA with Tukey's post hoc test. *p < 0.05; **p < 0.01; ***p <0.001; ****p < 0.0001; ns denotes no significance.

Figure 2. Loss of GHR in adipose tissue blunts insulin-driven lipogenesis in the liver of *L-Ghr*$^{-/-}$ mice.
a KEGG pathway enrichment analysis of differentially expressed genes (DEGs) with $|\log_2 FC| > 1$ in the liver, comparing *Ghr*$^{f/f}$ versus *L-Ghr*$^{-/-}$ (left), and *F/L-Ghr*$^{-/-}$ versus *L-Ghr*$^{-/-}$ (right). **b** DEGs in the indicated comparisons were shown in the scatter plot. Genes upregulated in *L-Ghr*$^{-/-}$ but downregulated in *F/L-Ghr*$^{-/-}$ were marked in red, whereas genes downregulated in *L-Ghr*$^{-/-}$ but upregulated in *F/L-Ghr*$^{-/-}$ were marked in blue (top). Venn diagram showing the overlap of DEGs marked in red scatterplot (bottom). **c** GSEA of DEGs showing upregulation of the lipogenesis pathway in *L-Ghr*$^{-/-}$ and its downregulation in *F/L-Ghr*$^{-/-}$. **d** Heatmap showing the top 27 DEGs that were upregulated in *L-Ghr*$^{-/-}$ but downregulated in *F/L-Ghr*$^{-/-}$. Lipogenesis-related genes were marked in red. n=6/group. **e** RT-qPCR analysis of core genes governing fatty-acid

uptake, fatty-acid oxidation, VLDL secretion and lipogenesis in livers from *Ghr*$^{f/f}$, *L-Ghr* $^{-/-}$, and *F/L-Ghr* $^{-/-}$ mice. n=8/group. **f** Representative immunoblots of lipogenesis-related proteins (ACC1, FAS, SCD1, and SREBP1) in liver lysates. Relative protein abundance quantified by image J was shown in the right panel. n=4 for representative samples. **g** Glucose tolerance test and corresponding area-under-curve (AUC) quantification. Blood glucose was measured at indicated times after i.p. glucose injection in 12-week-old male mice. Data are presented as means ± SEM. n=6/group. **h** Insulin tolerance test (ITT) with AUC statistics. Blood glucose was measured at indicated times after i.p. insulin injection in 12-week-old male mice. Data are presented as means ± SEM. n=6/group. **i** Circulating GH concentration measured in plasma samples. n=7/group. **j** Plasma insulin levels across three experimental genotypes. n=7/group. **k**. Representative images of H&E staining and insulin immunohistochemistry. Quantification of islet number was shown in the right panel. n=3/group. Scale bar, 500 μm for H&E staining; 1000 μm for immunohistochemistry. **l**. Representative images of H&E staining and insulin immunohistochemistry. Quantification of islet size was shown in the right panel. n=3/group. Scale bar, 100 μm. Data (f, i-l) are presented as individual values with the means. p values were determined by one-way ANOVA with Tukey's post hoc test. *p < 0.05; **p < 0.01; ***p <0.001; ****p < 0.0001; ns denotes no significance.

Figure 3. Elevated adipokine CFD promotes insulin secretion and hepatic steatosis in *L-Ghr* $^{-/-}$ mice.

a Representative images of developed protein chips incubated with plasma samples from *Ghr* $^{f/f}$, *L-Ghr* $^{-/-}$, and *F/L-Ghr* $^{-/-}$ mice. CFD is highlighted in a green box. n=7/group. **b** Immunoblot validation of CFD protein abundance in plasma samples (left); coomassie staining served as the loading control (right). **c** Plasma CFD protein levels in *Ghr*$^{f/f}$, *L-Ghr* $^{-/-}$, and *F/L-Ghr* $^{-/-}$ mice. n=7/group. **d** Circulating C3a protein levels in mice plasma. n=7/group. **e** RT-qPCR analysis of *Cfd* expression in adipose tissues, including epididymal WAT (eWAT), inguinal WAT (iWAT) and brown adipose tissue (BAT). n=7/group. **f** Immunoblot analysis of CFD protein in eWAT, iWAT and BAT across three genotypes. HSP90 was used as loading control. Relative protein abundance quantified by image J is shown in the right panel. n=4 for representative samples. **g** Immunohistochemical staining for CFD in adipose tissues sections. n=7/group. Scale bar, 100 μm. **h** *In-vivo* fluorescence imaging showing AAV signal intensity in the ventral and dorsal regions of experimental mice after in situ AAV injection. **i** Immunoblotting of CFD in adipose tissues from *L-Ghr* $^{-/-}$ mice injected with AAV expressing either control shRNA (Ctrl shRNA) or ap2-*Cfd* shRNA. Corresponding quantitative analysis is provided. n=4 for representative samples. **j** Plasma CFD (left) and plasma insulin (right) levels in *L-Ghr* $^{-/-}$ mice injected with Ctrl shRNA or ap2-*Cfd* shRNA AAV. n=6/group. **k** Representative images of H&E staining and insulin immunohistochemistry of pancreatic islets from *L-Ghr* $^{-/-}$ mice injected with Ctrl shRNA or ap2-*Cfd* shRNA, together with quantification of islet number and islet size. n=3/group. Scale bar, 1000 μm. **l** RT-qPCR analysis of hepatic lipogenic genes expression in *L-Ghr* $^{-/-}$ mice injected with Ctrl shRNA or ap2-*Cfd* shRNA. n=6/group.

m Immunoblot analysis of lipogenic proteins in liver lysates from Ctrl shRNA or ap2-*Cfd* shRNA treated *L-Ghr* $^{-/-}$ mice. Quantification using image J is shown in the right panel. n = 4 for representative samples. **n** Representative H&E and Oil-Red-O staining of liver sections from *L-Ghr* $^{-/-}$ mice injected with Ctrl shRNA or ap2-*Cfd* shRNA. n=4/group. Scale bar, 100 μm. **o** Hepatic triglyceride (TG) measurement in *L-Ghr* $^{-/-}$ mice injected with Ctrl shRNA or ap2-*Cfd* shRNA. n=7/group.
Data (c-f, i-m, o) are presented as individual values with the means. p values were determined by one-way ANOVA with Tukey's post hoc test (c-f), and unpaired Student's t test (i-m and o). *p < 0.05; **p < 0.01; ***p < 0.001; ****p < 0.0001; ns denotes no significance.

Figure 4. Attenuation of insulin-induced hepatic steatosis by CFD deficiency in DIO and *L-Ghr* $^{-/-}$ mice.
a Body-weight-tracking curve of wild-type (WT) and *Cfd* $^{-/-}$ mice during high-fat-diet (HFD) feeding. n=8/group. Data are presented as means ± SEM. **b** Plasma CFD levels in WT and *Cfd* $^{-/-}$ mice after 6 weeks of HFD feeding. n=8/group. **c** Plasma Insulin levels in WT and *Cfd* $^{-/-}$ mice after 6 weeks of HFD feeding. n=8/group. **d** Representative images of H&E staining and insulin immunohistochemistry in pancreatic sections from HFD-fed WT and *Cfd* $^{-/-}$ mice, with quantification of islet number. n=4/group. Scale bar, 500 μm for H&E staining; 1000 μm for immunohistochemistry. **e** Immunofluorescence images of pancreatic islets showing glucagon (red), insulin (green) and DAPI (blue). n=4/group. Scale bar, 100 μm. **f** Glucose tolerance test. Blood glucose was measured at indicated times after i.p. glucose injection in 8-week-old male mice fed HFD for 6 weeks. The corresponding AUC is shown. Data are presented as means ± SEM. n=8/group. **g** Insulin tolerance test. Blood glucose was measured at indicated times after i.p. insulin injection in male mice fed HFD for 6 weeks, and the corresponding AUC was quantified. Data are presented as means ± SEM. n=8/group. **h** Hepatic TG content in HFD-fed WT and *Cfd* $^{-/-}$ mice. n=8/group. **i** Liver H&E and Oil Red O staining in HFD-fed WT and *Cfd* $^{-/-}$ mice. n=4/group. Scale bar, 100 μm. **j** RT-qPCR analysis the expression of hepatic lipogenic genes in HFD-fed WT and *Cfd* $^{-/-}$ mice. n=6/group. **k** Immunoblot analysis of lipogenic proteins in HFD-fed WT and *Cfd* $^{-/-}$ mice. ImageJ quantification is shown on the right. n=4 for representative samples. **l** Immunoblot analysis of CFD protein levels in eWAT and iWAT from *L-Ghr* $^{-/-}$ and *L-Ghr* $^{-/-}$&*Cfd* $^{-/-}$ mice. Image J quantification is shown on the right. n=4 for representative samples. **m** Plasma CFD (left) and plasma insulin (right) levels in *L-Ghr* $^{-/-}$ and *L-Ghr* $^{-/-}$&*Cfd* $^{-/-}$ mice. n=7/group. **n** H&E staining and insulin immunohistochemistry of pancreatic sections, with quantification of islet number. n=4/group. Scale bar, 200 μm. **o** Liver H&E and Oil Red O staining. n=4/group. Scale bar, 100 μm. **p** Hepatic TG levels in *L-Ghr* $^{-/-}$ and *L-Ghr* $^{-/-}$&*Cfd* $^{-/-}$ mice. n=7/group. **q** RT-qPCR analysis of lipogenic genes mRNA in livers from *L-Ghr* $^{-/-}$ and *L-Ghr* $^{-/-}$&*Cfd* $^{-/-}$ mice. n=7/group. **r** Immunoblot analysis and quantification of lipogenesis-related proteins in liver lysates from *L-Ghr* $^{-/-}$ and *L-Ghr* $^{-/-}$&*Cfd* $^{-/-}$ mice. n=6 for representative samples.
Data (b-d, h, j-k, m-n, p-r) are presented as individual values with the means. p values

were determined by two-way ANOVA with Bonferroni's post hoc test (a), and unpaired Student's t test (b-d, h, j-k, m-n, p-r). *p < 0.05; **p < 0.01; ***p < 0.001; ****p < 0.0001; ns denotes no significance.

Figure 5. PPAR-γ and STAT5 collaboratively bind the *Cfd* promoter to activate transcription.

a Immunoblot analysis of STAT5 and CFD protein levels in eWAT from *Ghr*$^{f/f}$, *L-Ghr*$^{-/-}$, and *F/L-Ghr*$^{-/-}$ mice. n=3 for representative samples. **b** Immunoblot analysis of CFD, PPARγ, and STAT5 during SVF adipocyte differentiation (day 0, 2, 4, 6). **c** RT-qPCR analysis of *Cfd* mRNA in adipogenic differentiation of SVF treated with vehicle (V) or 1 μM T0070907 (T) or 100 μM STAT5-IN-1 (S). n=4/group. **d** Immunoblot analysis of CFD during adipogenic differentiation of SVF cells treated 1 μM T0070907 or 100 μM STAT5-IN-1. **e** Immunoblot analysis of CFD during adipogenic differentiation in SVF cells treated with control shRNA (sh Ctrl) or *Pparγ* shRNA (sh *Pparγ*). **f** Immunoblot analysis of CFD during adipogenic differentiation in SVF cells treated with siRNA targeting *Stat5a* or *Stat5b*. **g** CUT&Tag binding profiles of PPARγ and STAT5 in adipocytes derived from 3T3-L1 differentiation. Heatmap showing genome-wide peak density in the −5 to +5 kb region flanking the TSS. Scale bar indicates peak density. **h** CUT&Tag tracks of PPARγ and STAT5 at the *Cfd* gene locus. **i** Motif analysis of sequences bound by STAT5 and PPARγ, and prediction of their binding sites in promoter of *Cfd* by JASPAR. **j** Relative luciferase activity of reporters containing different *Cfd* promoter fragments upon PPARγ overexpression (left) or silencing (right). n=3-4/group. **k** Luciferase reporter assays of the *Cfd* promoter in 3T3-L1 cells treated with 1 μM T0070907 or 1 μM Pioglitazone (PIO). n=3/group. **l** Luciferase reporter assays of *Cfd* promoter activity in 3T3-L1 cells after STAT5A or STAT5B overexpression (left) or knockdown (right). n=4/group. **m** ChIP-qPCR in differentiation of 3T3-L1 cells. Enrichment of PPARγ or STAT5 at the *Cfd* promoter was detected relative to IgG control. n=3/group. **n** Co-IP analysis of the interaction between STAT5A and PPARγ (left) or STAT5B and PPARγ (right) in HEK293T cells co-overexpressing Flag-PPARγ and HA-STAT5A or HA-STAT5B. **o** Immunoblot analysis of CFD in 3T3-L1 cells overexpressing PPARγ with STAT5A or STAT5B knockdown. **p** Immunoblot analysis of CFD in 3T3-L1 cells overexpressing STAT5B, with or without PPARγ silencing.

Data (b, j-m) are presented as individual values with the means. p values were determined by one-way ANOVA with Tukey's post hoc test (b, k-i), two-way ANOVA followed by Bonferroni's post hoc test (j), and unpaired Student's t test (m). *p < 0.05; **p < 0.01; ***p < 0.001; ****p < 0.0001; ns denotes no significance.

Figure 6. GH-STAT5B signaling recruits PPAR-γ to the nucleus, where it drives CFD upregulation.

a Dual-luciferase reporter assays showing the effects of GH on *Cfd* promoter activity in 3T3-L1 cells co-overexpressing STAT5A (left) or STAT5B (right) together with PPARγ. n=4/group. **b** Co-IP analysis of the effects of GH on STAT5A–PPARγ and STAT5B–PPARγ interactions. **c** Co-IP analysis of the STAT5B–PPARγ interaction after

treatment with increasing GH doses. **d** Immunoblot analysis of total-cell lysates from 3T3-L1 cells transfected with control gRNA or *Ghr* gRNA after treatment with increasing doses of GH. **e** Immunoblot analysis of CFD in GH-treated 3T3-L1 cells with siRNA-mediated knockdown of *Stat5a* or *Stat5b*. **f** Immunoblotting of subcellular fractions from 3T3-L1 cells after treatment with increasing doses of GH. **g** Representative immunofluorescence images of PPARγ (green), STAT5B (red) and DAPI (blue) in 3T3-L1 cells with or without STAT5B-knockdown. n=3/group. Scale bar, 10 μm. **h** Confocal immunofluorescence images of 3T3-L1 cells overexpressed FLAG-PPARγ (green) and HA-STAT5B (red) in the presence or absence of GH. Fluorescence intensity was quantified using ImageJ. n=3/group. Scale bar, 20 μm. **i** Re-ChIP-qPCR analysis in 3T3-L1 cells showing co-occupancy of STAT5B (first IP) and PPARγ or IgG (second IP) at the *Cfd* locus after GH treatment. n=3/group. **j** ChIP-qPCR analysis of PPARγ or IgG enrichment at the *Cfd* locus with or without STAT5B knockdown. n=3/group. **k** Immunoblot analysis showing targeted proteins expression in 3T3-L1 cells after the indicated treatments.
Data (a, i-j) are presented as individual values with the means. p values were determined by one-way ANOVA with Tukey's post hoc test (a), and two-way ANOVA followed by Bonferroni's post hoc test (i-j). *p < 0.05; **p < 0.01; ***p < 0.001; ****p < 0.0001; ns denotes no significance. Data are representative of at least two independent experiments.

Figure 7. CFD acts on islets to enhance insulin secretion via EV-mediated delivery. **a** GSIS in isolated mouse islets under recombinant CFD protein treatment. n=6/group. **b** Schematic workflow for isolating two EV populations from mouse blood by sequential differential ultracentrifugation (crude EVs/ 1st EVs and refined EVs/ 2nd EVs). **c** NTA showing particle-size distribution of isolated 1st EVs and 2nd EVs from *Ghr*$^{f/f}$, *L-Ghr* $^{-/-}$, and *F/L-Ghr* $^{-/-}$ mice plasma. **d** TEM image of 1st EVs and 2nd EVs from plasma. Scale bar, 100 nm. **e** Immunoblot of CFD and EV marker proteins CD9 and ALIX; Calnexin (CANX) as negative control in 1st EVs and 2nd EVs derived from plasma of three genotypes. **f** GSIS (left) and ATP/ADP ratio (right) in primary pancreatic islets treated with 1st EVs or 2nd EVs isolated from plasma of *Ghr*$^{f/f}$, *L-Ghr* $^{-/-}$, and *F/L-Ghr* $^{-/-}$ mice. n=6/group. **g** Intracellular calcium measurements and immunofluorescence images of primary pancreatic islets following EV stimulation as indicated. n=6/group. Scale bar, 10 μm. **h** Experimental scheme for generating recombinant CFD-loaded EVs (CFD EVs) by electroporation. **i** NTA particle-size profiles of control EVs and CFD EVs. **j** TEM micrographs of control EVs and CFD EVs. Scale bar, 100 nm. **k** GSIS, ATP/ADP ration, and intracellular calcium assay in isolated mouse islets incubated with control EVs or CFD EVs. n=6/group. **l** Real-time recording of oxygen consumption rate (OCR) in Min6 cells treated with control EVs or CFD EVs, following sequential addition of oligomycin, FCCP and rotenone-antimycin A. Data are presented as means ± SD. n=4/group. **m** Quantification of basal respiration, ATP-linked respiration and maximal respiration calculated from OCR traces. n=4/group. **n** Schematic diagram illustrating pancreatic ductal infusion of EVs in *Cfd* $^{-/-}$ mice. **o** Representative immunofluorescence images showing the expression of insulin in

pancreatic islets after pancreatic ductal infusion of control EVs or CFD-EVs. n=6/group. Scale bar, 20 μm. **p** Plasma insulin levels in recipient mice after pancreatic ductal infusion of control EVs or CFD-EVs. n=7/group.
Data (a, f-g, k, m, o-p) are presented as individual values with the means. p values were determined by one-way ANOVA with Tukey's post hoc test (f-g), and two-way ANOVA followed by Bonferroni's post hoc test (a, k), and unpaired Student's t test (m, o-p). *p < 0.05; **p < 0.01; ***p < 0.001; ****p < 0.0001; ns denotes no significance.

Figure 8. Effects of CFD-associated inhibitors on *L-Ghr*$^{-/-}$ mice.
a Schematic of the FD-IN-1 administration workflow in *L-Ghr*$^{-/-}$ mice. **b** Immunoblot analysis of CFD protein in eWAT from *L-Ghr*$^{-/-}$ mice treated with vehicle or FD-IN-1. n=4 for representative samples. **c** Plasma CFD (left) and plasma insulin (right) levels in the same treated mice. n=6/group. **d** Representative pancreatic H&E and insulin immunohistochemical staining with quantification of islet number. n=6/group. Scale bar, 200 μm. **e** Liver H&E and Oil Red O staining of mice treated with vehicle or FD-IN-1. n=4/group. Scale bar, 100 μm. **f** Hepatic triglyceride content in the same mice. n=6/group. **g** RT-qPCR analysis of related hepatic lipogenic genes. n=6/group. **h** Immunoblot analysis of lipogenesis-related proteins in liver lysates, with quantification using ImageJ. n=4 for representative samples. **i** Schematic of GW4869 treatment in *L-Ghr*$^{-/-}$ mice. **j** Immunoblot of CFD protein in eWAT from *L-Ghr*$^{-/-}$ mice treated with vehicle or GW4869. n=5 for representative samples. **k** Plasma CFD (left) and plasma insulin (right) levels in the same mice treated as in (j). n=5/group. **l** Pancreatic H&E and insulin immunohistochemistry with quantification of islet number. n=5/group. Scale bar, 200 μm. **m** Liver H&E and Oil Red O staining. n=4/group. Scale bar, 100 μm. **n** Hepatic triglyceride content in the same treated mice. n=5/group. **o** RT-qPCR analysis of hepatic lipogenic-gene expression. n=5/group. **p** Immunoblot and quantitative analysis of hepatic lipogenic proteins. n=3 for representative samples. **q** Schematic of STAT5-inhibitor STAT-IN-1 or vehicle in-situ injection in *L-Ghr*$^{-/-}$ mice. **r** Immunoblot showing CFD protein in eWAT after STAT-IN-1 injection. n=5 for representative samples. **s** Plasma CFD (left) and plasma insulin (right) levels in the same mice treated as in (r). n=5/group. **t** Pancreatic H&E and insulin immunohistochemistry, with quantification of islet number. n=5/group. Scale bar, 200 μm. **u** Liver H&E and Oil Red O staining. Scale bar, 100 μm. **v** Hepatic triglyceride levels in the same treated mice. n=5/group. **w** RT-qPCR analysis of hepatic related lipogenic genes expression. n=5/group. **x** Immunoblot analysis of lipogenesis-related proteins in liver lysates, with quantification using ImageJ. n=5 for representative samples.
Data (c-d, f-h, k-l, n-p, s-t, v-x) are presented as individual values with the means. p values were determined by unpaired Student's t test. *p < 0.05; **p < 0.01; ***p < 0.001; ****p < 0.0001; ns denotes no significance.

Figure 9. CFD in circulating EVs is positively associated with hepatic steatosis in patients with MASLD.
a Representative image of H&E-stained liver sections from human subjects with varying degrees of hepatic lipid accumulation. n=6/group. Scale bar, 50 μm. **b** Plasma

ALT levels in human subjects with moderate (n = 21) or severe (n = 10) hepatic steatosis compared with healthy individuals (n = 18). **c** Plasma insulin levels in the same human subjects. **d** Plasma CFD levels in the same human subjects. **e** Scatter plots showing the positive correlation between plasma ALT and insulin levels. **f** Scatter plots illustrating the positive correlations between plasma ALT and CFD levels (left) and between plasma insulin and CFD levels (right) in human subjects. Pearson correlation coefficients R and corresponding P values are indicated. **g** ROC curve analysis of logistic regression (Logi) models using plasma ALT, plasma insulin, plasma CFD, or a combined three-marker panel to distinguish subjects with hepatic steatosis from normal controls. **h** NTA profiles of 1st-EV and 2nd-EV fractions isolated from plasma samples across different hepatic steatosis grades. **i** TEM images of 1st EVs and 2nd EVs as in (h). Scale bar, 100 nm. **j** Immunoblot analysis of CFD, EV marker TSG101 and negative control CANX in human plasma-derived 1st-EV and 2nd-EV fractions from normal, moderate-fat and high-fat subjects. **k** ELISA measurement of CFD distribution in 1st-EVs, 2nd-EVs and EVs-depleted supernatant fractions (left). Relative proportion of EV-bound CFD versus total circulating CFD in human plasma across hepatic fat grades(right). n=5/group.

Data (b-d, k) are presented as individual values with the means. p values were determined by one-way ANOVA with Tukey's post hoc test, and Pearson test was used for correlation analysis. *p < 0.05; **p < 0.01; ***p < 0.001; ****p < 0.0001; ns denotes no significance.

Figure 10. Schematic model of the growth hormone–CFD–insulin axis in liver steatosis.

In *L-Ghr* $^{-/-}$ mice, elevated GH acts on adipose tissue to promote PPARγ–STAT5B cooperation at the *Cfd* promoter, thereby increasing *Cfd* transcription and CFD production. CFD is packaged into extracellular vesicles, which deliver CFD to pancreatic islets, enhancing β-cell mitochondrial respiration, ATP production, and Ca^{2+} influx, thereby potentiating GSIS. The resulting increase in insulin secretion contributes to hepatic DNL and lipid accumulation. Pharmacological inhibition of CFD activity, EV secretion, or adipose CFD production alleviates hepatic steatosis in *L-Ghr* $^{-/-}$ mice.

Figures for

Adipose extracellular vesicle CFD in growth hormone–driven insulin-dependent hepatic steatosis

Peng Wei[1,2,4], Junliang Chen[1,2,4], Tong Wu[2,4], Chengying Xu[2], Yajie Wang[2], Yingjie Zhang[2], Kejian Wei[2], Fei Gao[2], Longlong Wang[2], Guocai Duan[2], Rui Zhao[2], Chuang Liu[2], Tao Wan[1,2,*], Zhonghua Lu[3,*], Fei Fang[1,2,5,*]

[1]Affiliated Hospital of Jiangnan University, Wuxi 214122, China

[2]Wuxi School of Medicine, Jiangnan University, Wuxi 214122, China

[3]Department of Infectious Diseases, Affiliated Hospital of Nantong University, Nantong, Jiangsu 226001, China

[4]These authors contributed equally

[5]Lead contract

*Correspondence: 8202304002@jiangnan.edu.cn, Lu_z_h@126.com, feifang@jiangnan.edu.cn

Address for lead contract:

Fei Fang, Ph.D., Wuxi School of Medicine, Jiangnan University, 1800 Lihu Road, Wuxi 214122, China.

Fig 1

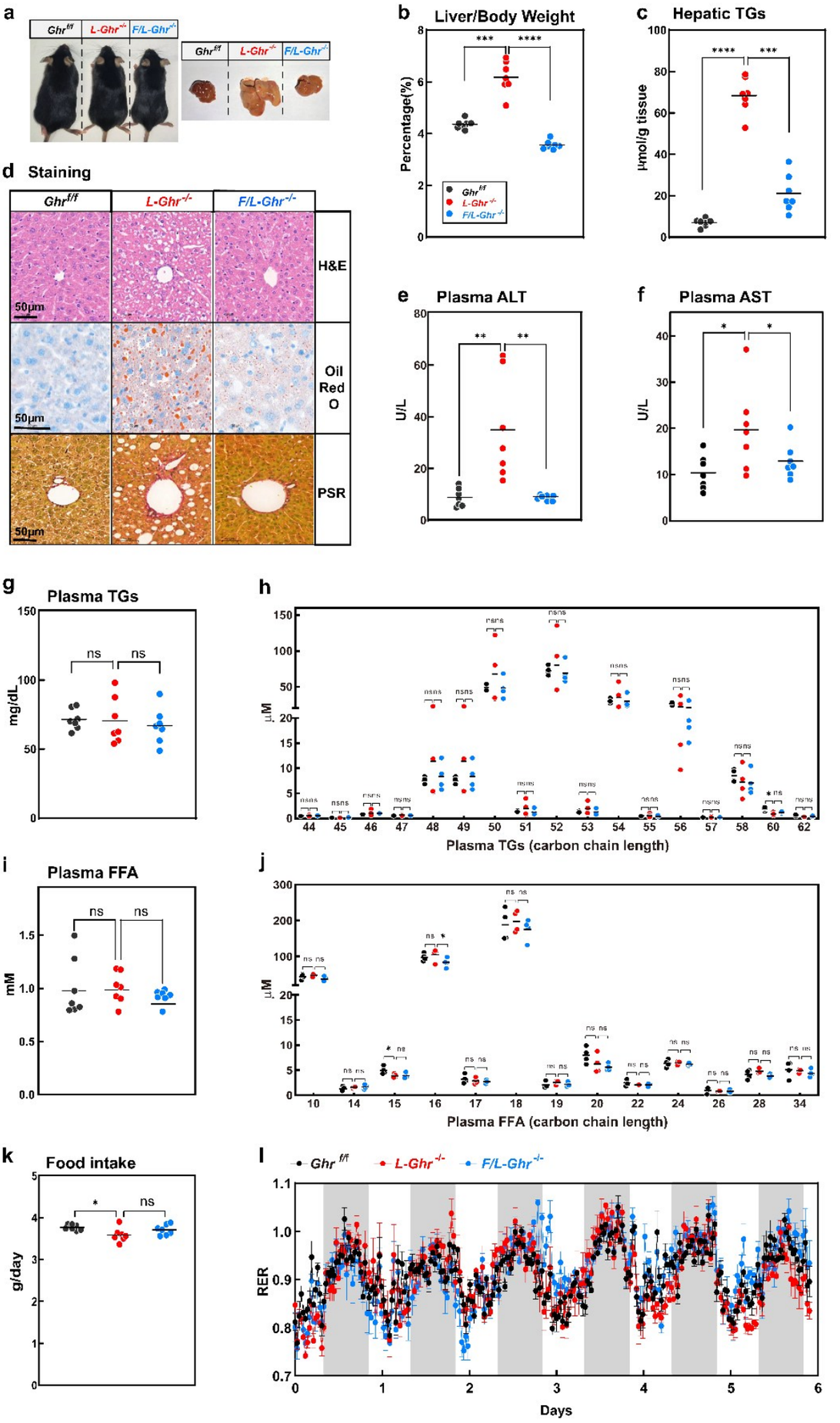

a
Ghr f/f
L-Ghr -/-
F/L-Ghr -/-
b Liver/Body Weight
Percentage(%)
c Hepatic TGs
μmol/g tissue
d Staining
H&E
Oil Red O
PSR
50μm
e Plasma ALT
U/L
f Plasma AST
U/L
g Plasma TGs
mg/dL
h
μM
Plasma TGs (carbon chain length)
i Plasma FFA
mM
j
μM
Plasma FFA (carbon chain length)
k Food intake
g/day
l
RER
Days

Fig 2

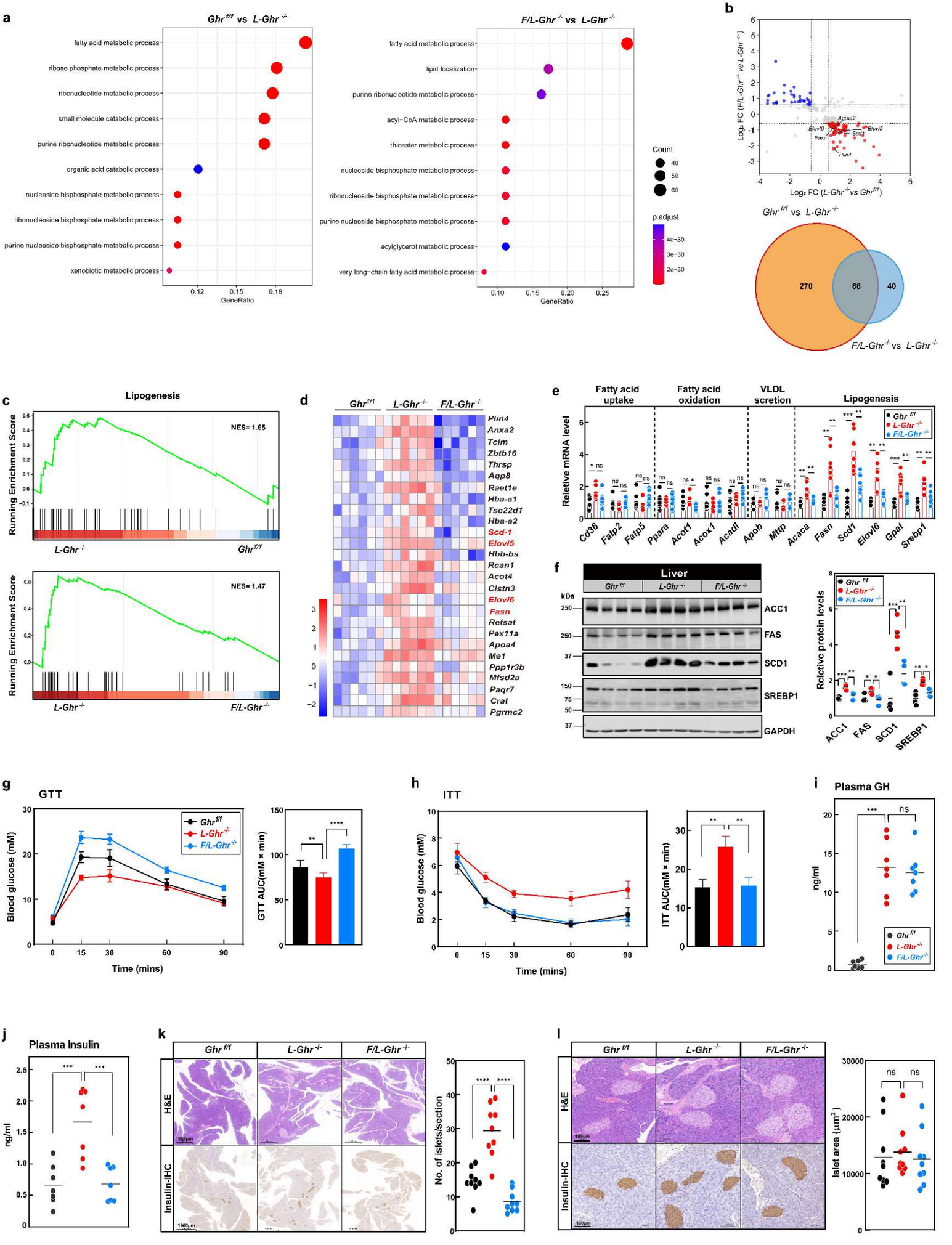

a
Ghr f/f vs L-Ghr -/-
fatty acid metabolic process
ribose phosphate metabolic process
ribonucleotide metabolic process
small molecule catabolic process
purine ribonucleotide metabolic process
organic acid catabolic process
nucleoside bisphosphate metabolic process
ribonucleoside bisphosphate metabolic process
purine nucleoside bisphosphate metabolic process
xenobiotic metabolic process
GeneRatio
F/L-Ghr -/- vs L-Ghr -/-
fatty acid metabolic process
lipid localization
purine ribonucleotide metabolic process
acyl-CoA metabolic process
thioester metabolic process
nucleoside bisphosphate metabolic process
ribonucleoside bisphosphate metabolic process
purine nucleoside bisphosphate metabolic process
acylglycerol metabolic process
very long-chain fatty acid metabolic process
GeneRatio
Count
p.adjust
b
Log2 FC (F/L-Ghr -/- vs L-Ghr -/-)
Log2 FC (L-Ghr -/- vs Ghr f/f)
Aqp12
Elovl6
Elovl5
Fasn
Scd1
Plin4
Ghr f/f vs L-Ghr -/-
270
68
40
F/L-Ghr -/- vs L-Ghr -/-
c
Lipogenesis
NES= 1.65
Running Enrichment Score
L-Ghr -/-
Ghr f/f
NES= 1.47
Running Enrichment Score
L-Ghr -/-
F/L-Ghr -/-
d
Ghr f/f
L-Ghr -/-
F/L-Ghr -/-
Plin4
Anxa2
Tcim
Zbtb16
Thrsp
Aqp8
Raet1e
Hba-a1
Tsc22d1
Hba-a2
Scd-1
Elovl5
Hbb-bs
Rcan1
Acot4
Clstn3
Elovl6
Fasn
Retsat
Pex11a
Apoa4
Me1
Ppp1r3b
Mfsd2a
Paqr7
Crat
Pgrmc2
e
Fatty acid uptake
Fatty acid oxidation
VLDL scretion
Lipogenesis
Relative mRNA level
Ghr f/f
L-Ghr -/-
F/L-Ghr -/-
Cd36
Fatp2
Fatp5
Ppara
Acot1
Acox1
Acadl
Apob
Mttp
Acaca
Fasn
Scd1
Elovl6
Gpat
Srebp1
f
Liver
Ghr f/f
L-Ghr -/-
F/L-Ghr -/-
kDa
ACC1
FAS
SCD1
SREBP1
GAPDH
Relative protein levels
ACC1
FAS
SCD1
SREBP1
g
GTT
Blood glucose (mM)
Time (mins)
GTT AUC(mM × min)
h
ITT
Blood glucose (mM)
Time (mins)
ITT AUC(mM × min)
i
Plasma GH
ng/ml
j
Plasma Insulin
ng/ml
k
H&E
Insulin-IHC
No. of islets/section
l
H&E
Insulin-IHC
Islet area (μm2)

Fig 3

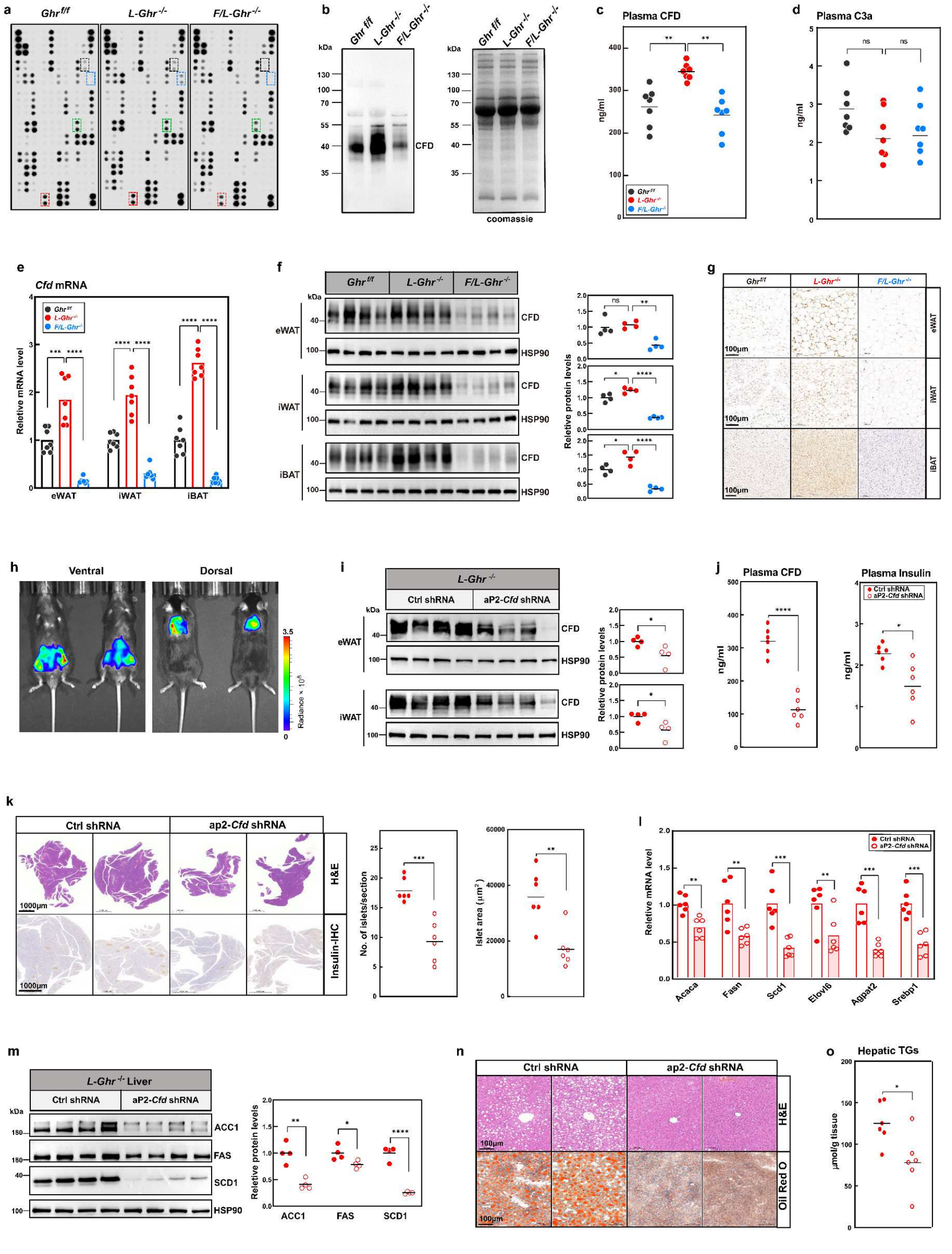

a
Ghr f/f
L-Ghr -/-
F/L-Ghr -/-
b
kDa
130
100
70
55
40
35
CFD
coomassie
c
Plasma CFD
ng/ml
d
Plasma C3a
ns
e
Cfd mRNA
Reletive mRNA level
eWAT
iWAT
iBAT
f
CFD
HSP90
Reletive protein levels
g
100μm
h
Ventral
Dorsal
Radiance × 10^6
i
Ctrl shRNA
aP2-Cfd shRNA
j
Plasma CFD
Plasma Insulin
k
H&E
Insulin-IHC
1000μm
No. of islets/section
Islet area (μm²)
l
Reletive mRNA level
Acaca
Fasn
Scd1
Elovl6
Agpat2
Srebp1
m
ACC1
FAS
SCD1
n
Oil Red O
o
Hepatic TGs
μmol/g tissue

Fig 4

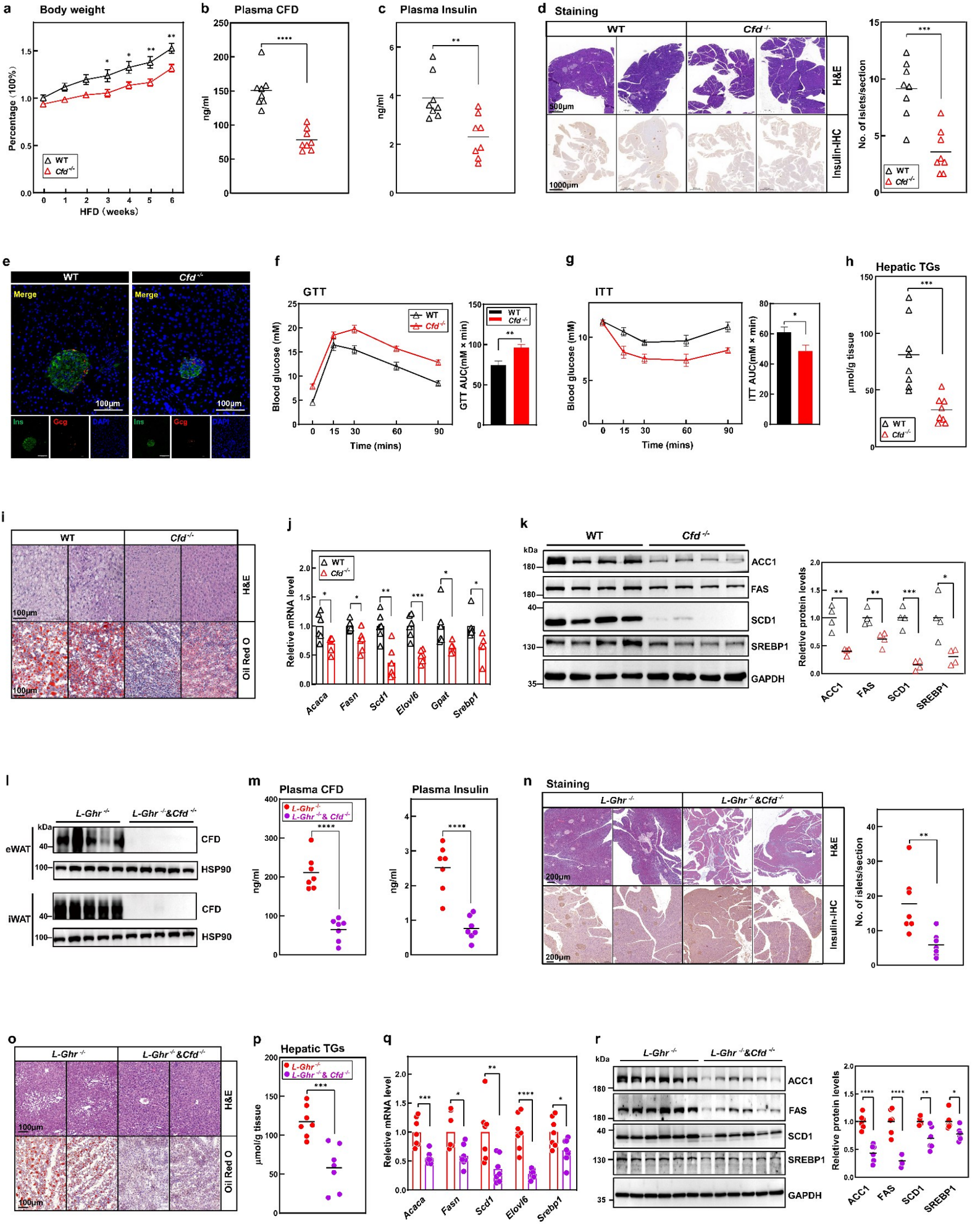

a
Body weight
Percentage (100%)
HFD (weeks)
WT
Cfd-/-
b
Plasma CFD
ng/ml
c
Plasma Insulin
ng/ml
d
Staining
WT
Cfd-/-
H&E
Insulin-IHC
500μm
1000μm
No. of islets/section
e
WT
Cfd-/-
Merge
100μm
Ins
Gcg
DAPI
f
GTT
Blood glucose (mM)
Time (mins)
GTT AUC(mM × min)
g
ITT
Blood glucose (mM)
Time (mins)
ITT AUC(mM × min)
h
Hepatic TGs
μmol/g tissue
i
WT
Cfd-/-
H&E
Oil Red O
100μm
j
Reletive mRNA level
Acaca
Fasn
Scd1
Elovl6
Gpat
Srebp1
k
WT
Cfd-/-
kDa
ACC1
FAS
SCD1
SREBP1
GAPDH
Reletive protein levels
l
L-Ghr-/-
L-Ghr-/-&Cfd-/-
eWAT
iWAT
CFD
HSP90
m
Plasma CFD
Plasma Insulin
L-Ghr-/-
L-Ghr-/-& Cfd-/-
ng/ml
n
Staining
L-Ghr-/-
L-Ghr-/-&Cfd-/-
H&E
Insulin-IHC
200μm
No. of islets/section
o
L-Ghr-/-
L-Ghr-/-&Cfd-/-
H&E
Oil Red O
100μm
p
Hepatic TGs
μmol/g tissue
q
Reletive mRNA level
Acaca
Fasn
Scd1
Elovl6
Srebp1
r
L-Ghr-/-
L-Ghr-/-&Cfd-/-
kDa
ACC1
FAS
SCD1
SREBP1
GAPDH
Reletive protein levels

Fig 5

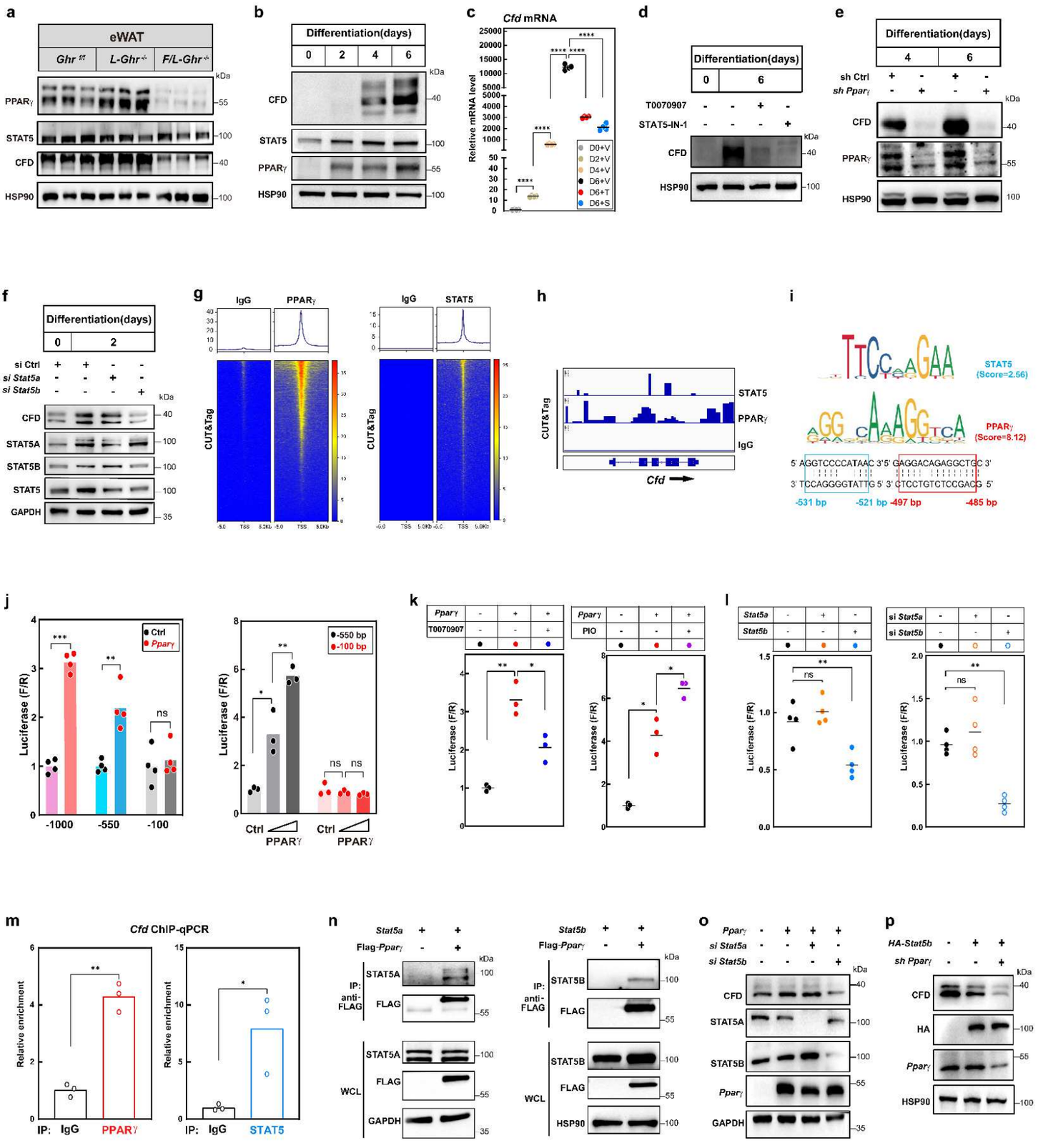

a
eWAT
Ghr f/f
L-Ghr-/-
F/L-Ghr-/-
kDa
PPARγ
STAT5
CFD
HSP90
55
100
40
100
b
Differentiation(days)
0
2
4
6
kDa
CFD
STAT5
PPARγ
HSP90
40
100
55
100
c
Cfd mRNA
Reletive mRNA level
D0+V
D2+V
D4+V
D6+V
D6+T
D6+S
d
Differentiation(days)
0
6
T0070907
STAT5-IN-1
kDa
CFD
HSP90
40
100
e
Differentiation(days)
4
6
sh Ctrl
sh Pparγ
kDa
CFD
PPARγ
HSP90
40
55
100
f
Differentiation(days)
0
2
si Ctrl
si Stat5a
si Stat5b
kDa
CFD
STAT5A
STAT5B
STAT5
GAPDH
40
100
100
100
35
g
IgG
PPARγ
IgG
STAT5
CUT&Tag
CUT&Tag
h
CUT&Tag
STAT5
PPARγ
IgG
Cfd
i
STAT5
(Score=2.56)
PPARγ
(Score=8.12)
5' AGGTCCCCATAAC 3'
3' TCCAGGGGTATTG 5'
5' GAGGACAGAGGCTGC 3'
3' CTCCTGTCTCCGACG 5'
-531 bp
-521 bp
-497 bp
-485 bp
j
Ctrl
Pparγ
Luciferase (F/R)
-1000
-550
-100
-550 bp
-100 bp
Ctrl
PPARγ
Ctrl
PPARγ
k
Pparγ
T0070907
Pparγ
PIO
Luciferase (F/R)
Luciferase (F/R)
l
Stat5a
Stat5b
si Stat5a
si Stat5b
Luciferase (F/R)
Luciferase (F/R)
m
Cfd ChIP-qPCR
Relative enrichment
IP: IgG
PPARγ
Relative enrichment
IP: IgG
STAT5
n
Stat5a
Flag-Pparγ
kDa
IP: anti-FLAG
STAT5A
FLAG
WCL
STAT5A
FLAG
GAPDH
100
55
100
55
35
Stat5b
Flag-Pparγ
kDa
IP: anti-FLAG
STAT5B
FLAG
WCL
STAT5B
FLAG
HSP90
100
55
100
55
100
o
Pparγ
si Stat5a
si Stat5b
kDa
CFD
STAT5A
STAT5B
Pparγ
GAPDH
40
100
100
55
35
p
HA-Stat5b
sh Pparγ
kDa
CFD
HA
Pparγ
HSP90
40
100
55
100

Fig 6

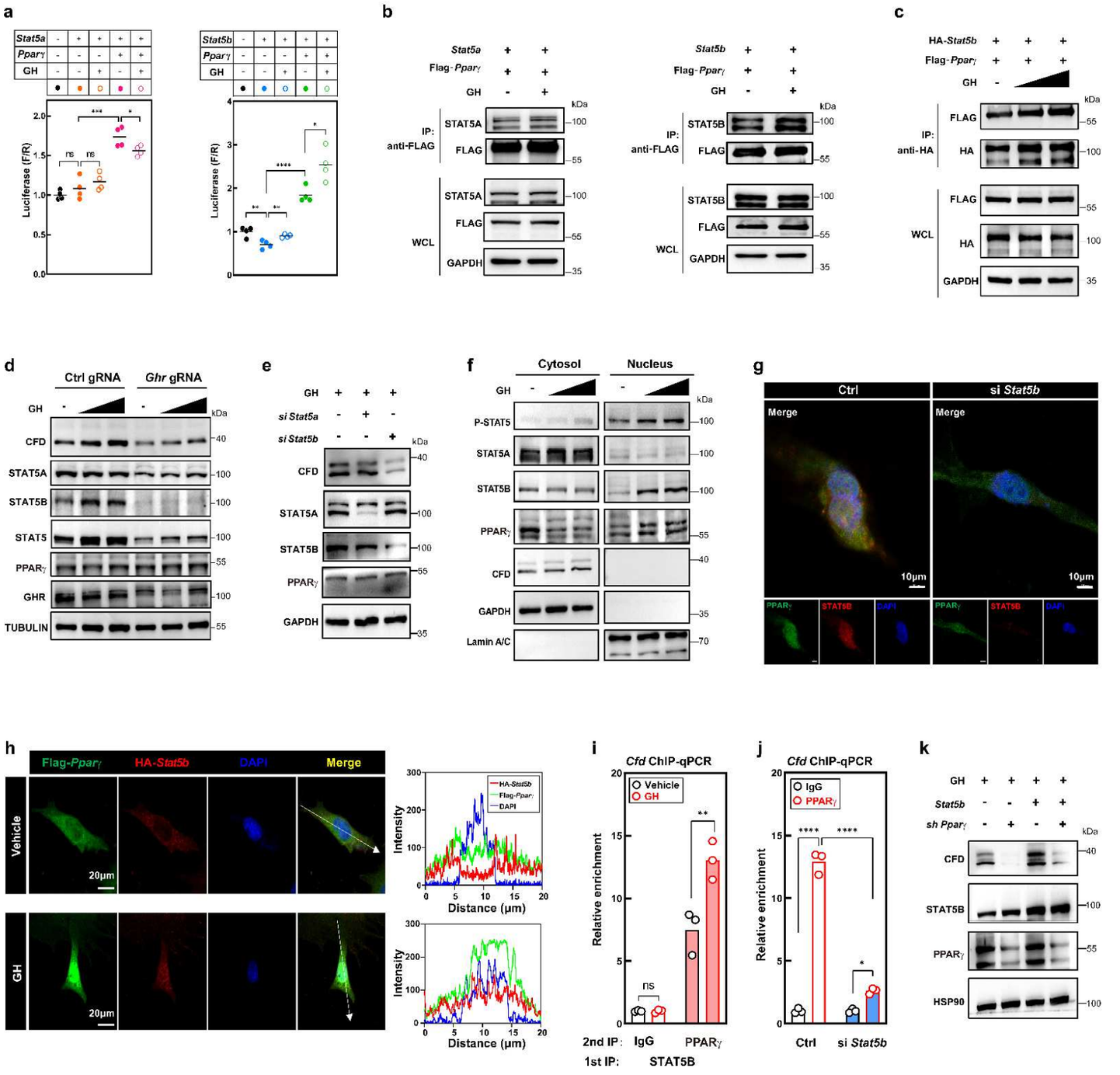
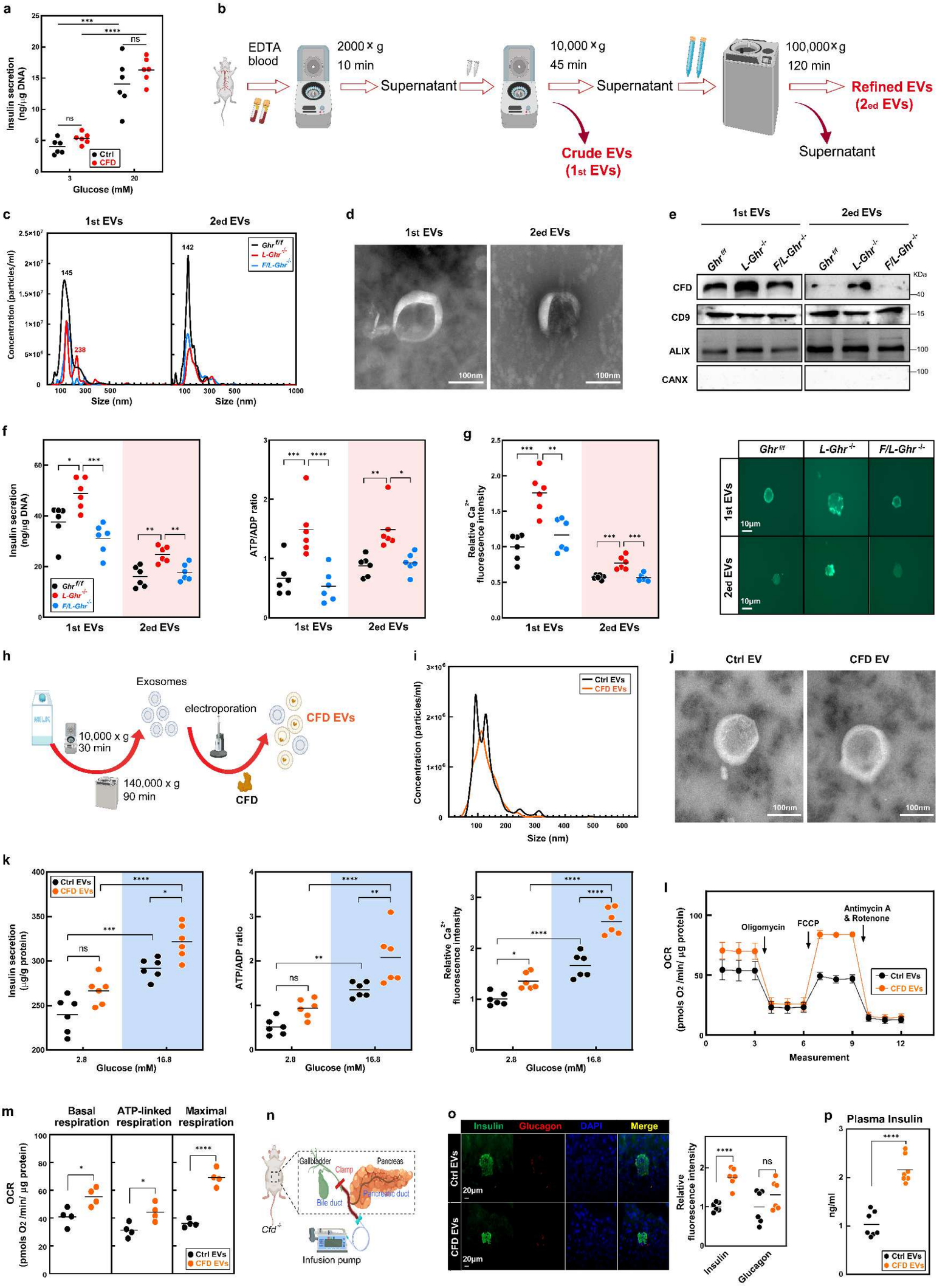

a
Stat5a
Pparγ
GH
Luciferase (F/R)
ns
ns
***
*
Stat5b
Pparγ
GH
Luciferase (F/R)
**
**
****
*
b
Stat5a
Flag-Pparγ
GH
kDa
IP: anti-FLAG
STAT5A
FLAG
WCL
STAT5A
FLAG
GAPDH
Stat5b
Flag-Pparγ
GH
kDa
IP: anti-FLAG
STAT5B
FLAG
WCL
STAT5B
FLAG
GAPDH
c
HA-Stat5b
Flag-Pparγ
GH
kDa
IP: anti-HA
FLAG
HA
WCL
FLAG
HA
GAPDH
d
Ctrl gRNA
Ghr gRNA
GH
kDa
CFD
STAT5A
STAT5B
STAT5
PPARγ
GHR
TUBULIN
e
GH
si Stat5a
si Stat5b
kDa
CFD
STAT5A
STAT5B
PPARγ
GAPDH
f
Cytosol
Nucleus
GH
kDa
P-STAT5
STAT5A
STAT5B
PPARγ
CFD
GAPDH
Lamin A/C
g
Ctrl
si Stat5b
Merge
10μm
PPARγ
STAT5B
DAPI
h
Flag-Pparγ
HA-Stat5b
DAPI
Merge
Vehicle
GH
20μm
HA-Stat5b
Flag-Pparγ
DAPI
Intensity
Distance (μm)
i
Cfd ChIP-qPCR
Vehicle
GH
Relative enrichment
ns
**
2nd IP: IgG PPARγ
1st IP: STAT5B
j
Cfd ChIP-qPCR
IgG
PPARγ
Relative enrichment
****
****
*
Ctrl
si Stat5b
k
GH
Stat5b
sh Pparγ
kDa
CFD
STAT5B
PPARγ
HSP90

Fig 7


a
Insulin secretion (ng/μg DNA)
Glucose (mM)
Ctrl
CFD
ns
b
EDTA blood
2000 × g
10 min
Supernatant
10,000 × g
45 min
Crude EVs (1st EVs)
100,000 × g
120 min
Refined EVs (2ed EVs)
c
1st EVs
2ed EVs
Concentration (particles/ml)
Size (nm)
d
1st EVs
2ed EVs
100nm
e
1st EVs
2ed EVs
CFD
CD9
ALIX
CANX
KDa
f
Insulin secretion (ng/μg DNA)
ATP/ADP ratio
1st EVs
2ed EVs
g
Relative Ca2+ fluorescence intensity
10μm
h
Exosomes
electroporation
CFD EVs
10,000 x g
30 min
140,000 x g
90 min
CFD
i
Ctrl EVs
CFD EVs
Concentration (particles/ml)
Size (nm)
j
Ctrl EV
CFD EV
100nm
k
Insulin secretion (μg/g protein)
ATP/ADP ratio
Relative Ca2+ fluorescence intensity
Glucose (mM)
l
OCR (pmols O2 /min/ μg protein)
Oligomycin
FCCP
Antimycin A & Rotenone
Measurement
m
Basal respiration
ATP-linked respiration
Maximal respiration
n
Gallbladder
Clamp
Pancreas
Bile duct
Pancreatic duct
Infusion pump
o
Insulin
Glucagon
DAPI
Merge
Ctrl EVs
CFD EVs
20μm
Relative fluorescence intensity
p
Plasma Insulin
ng/ml

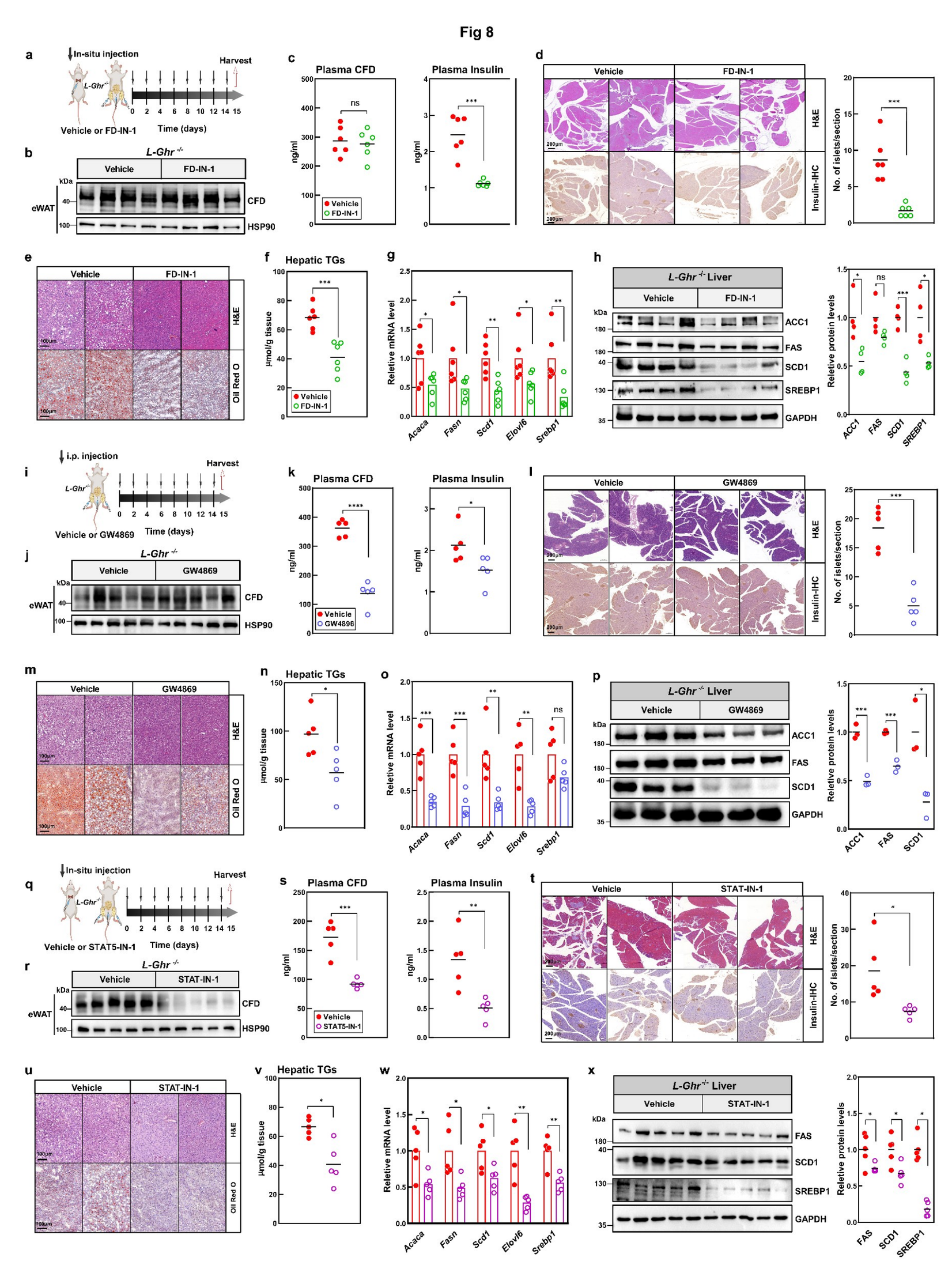

Fig 8
a
In-situ injection
Harvest
L-Ghr-/-
0 2 4 6 8 10 12 14 15
Vehicle or FD-IN-1
Time (days)
b
L-Ghr -/-
Vehicle
FD-IN-1
kDa
eWAT
40
100
CFD
HSP90
c
Plasma CFD
ns
ng/ml
Vehicle
FD-IN-1
Plasma Insulin
***
ng/ml
d
Vehicle
FD-IN-1
H&E
Insulin-IHC
200μm
No. of islets/section
***
e
Vehicle
FD-IN-1
H&E
Oil Red O
100μm
f
Hepatic TGs
***
μmol/g tissue
Vehicle
FD-IN-1
g
Reletive mRNA level
Acaca
Fasn
Scd1
Elovl6
Srebp1
h
L-Ghr -/- Liver
Vehicle
FD-IN-1
kDa
180
40
130
35
ACC1
FAS
SCD1
SREBP1
GAPDH
Reletive protein levels
ns
i
i.p. injection
Harvest
L-Ghr-/-
0 2 4 6 8 10 12 14 15
Vehicle or GW4869
Time (days)
j
L-Ghr -/-
Vehicle
GW4869
kDa
eWAT
40
100
CFD
HSP90
k
Plasma CFD
****
ng/ml
Vehicle
GW4896
Plasma Insulin
*
ng/ml
l
Vehicle
GW4869
H&E
Insulin-IHC
200μm
No. of islets/section
***
m
Vehicle
GW4869
H&E
Oil Red O
100μm
n
Hepatic TGs
*
μmol/g tissue
o
Reletive mRNA level
***
**
ns
Acaca
Fasn
Scd1
Elovl6
Srebp1
p
L-Ghr -/- Liver
Vehicle
GW4869
kDa
180
40
35
ACC1
FAS
SCD1
GAPDH
Reletive protein levels
q
In-situ injection
Harvest
L-Ghr-/-
0 2 4 6 8 10 12 14 15
Vehicle or STAT5-IN-1
Time (days)
r
L-Ghr -/-
Vehicle
STAT-IN-1
kDa
eWAT
40
100
CFD
HSP90
s
Plasma CFD
***
ng/ml
Vehicle
STAT5-IN-1
Plasma Insulin
**
ng/ml
t
Vehicle
STAT-IN-1
H&E
Insulin-IHC
200μm
No. of islets/section
*
u
Vehicle
STAT-IN-1
H&E
Oil Red O
100μm
v
Hepatic TGs
*
μmol/g tissue
w
Reletive mRNA level
Acaca
Fasn
Scd1
Elovl6
Srebp1
x
L-Ghr -/- Liver
Vehicle
STAT-IN-1
kDa
180
40
130
35
FAS
SCD1
SREBP1
GAPDH
Reletive protein levels
FAS
SCD1
SREBP1

Fig 9

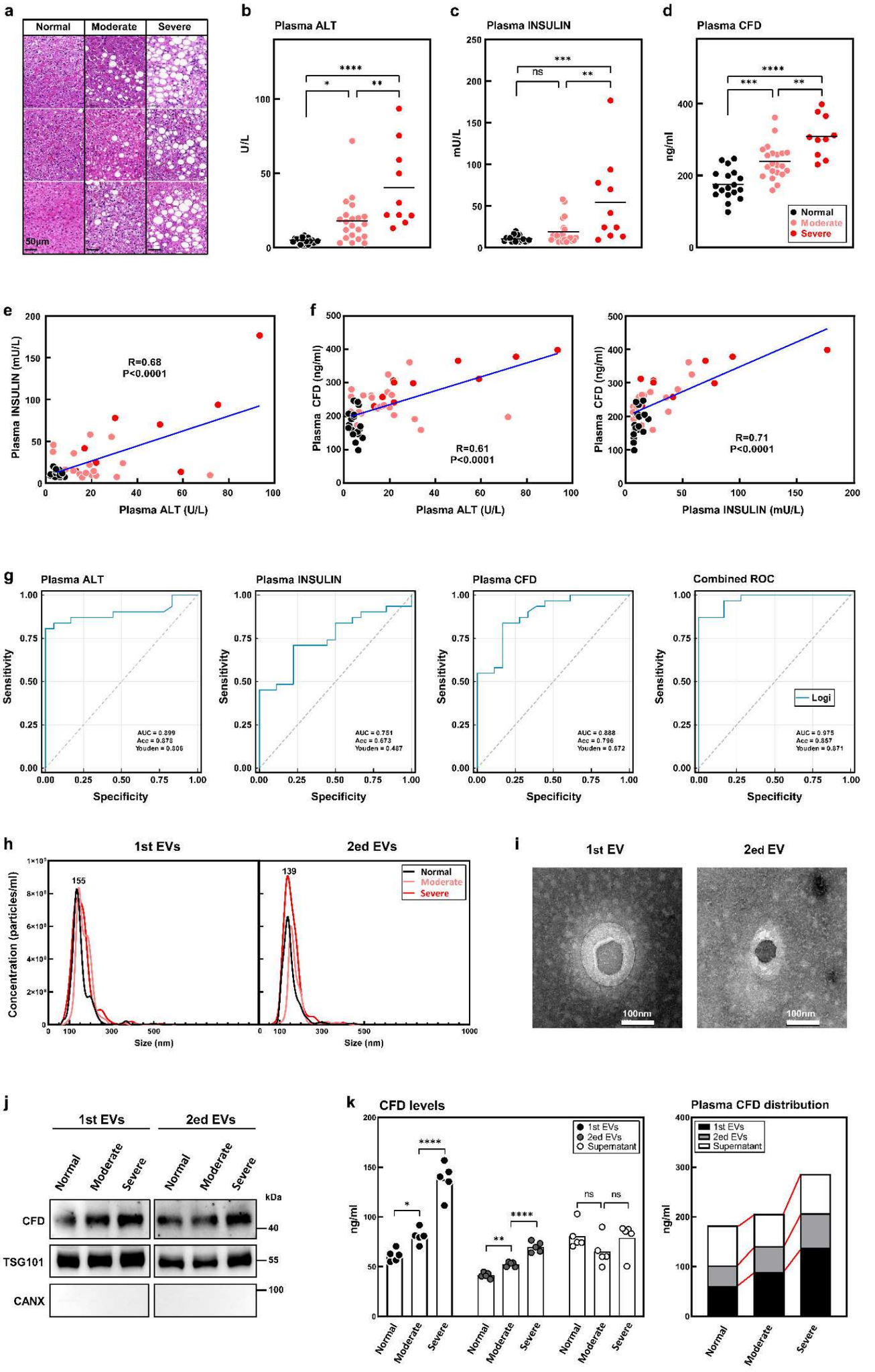
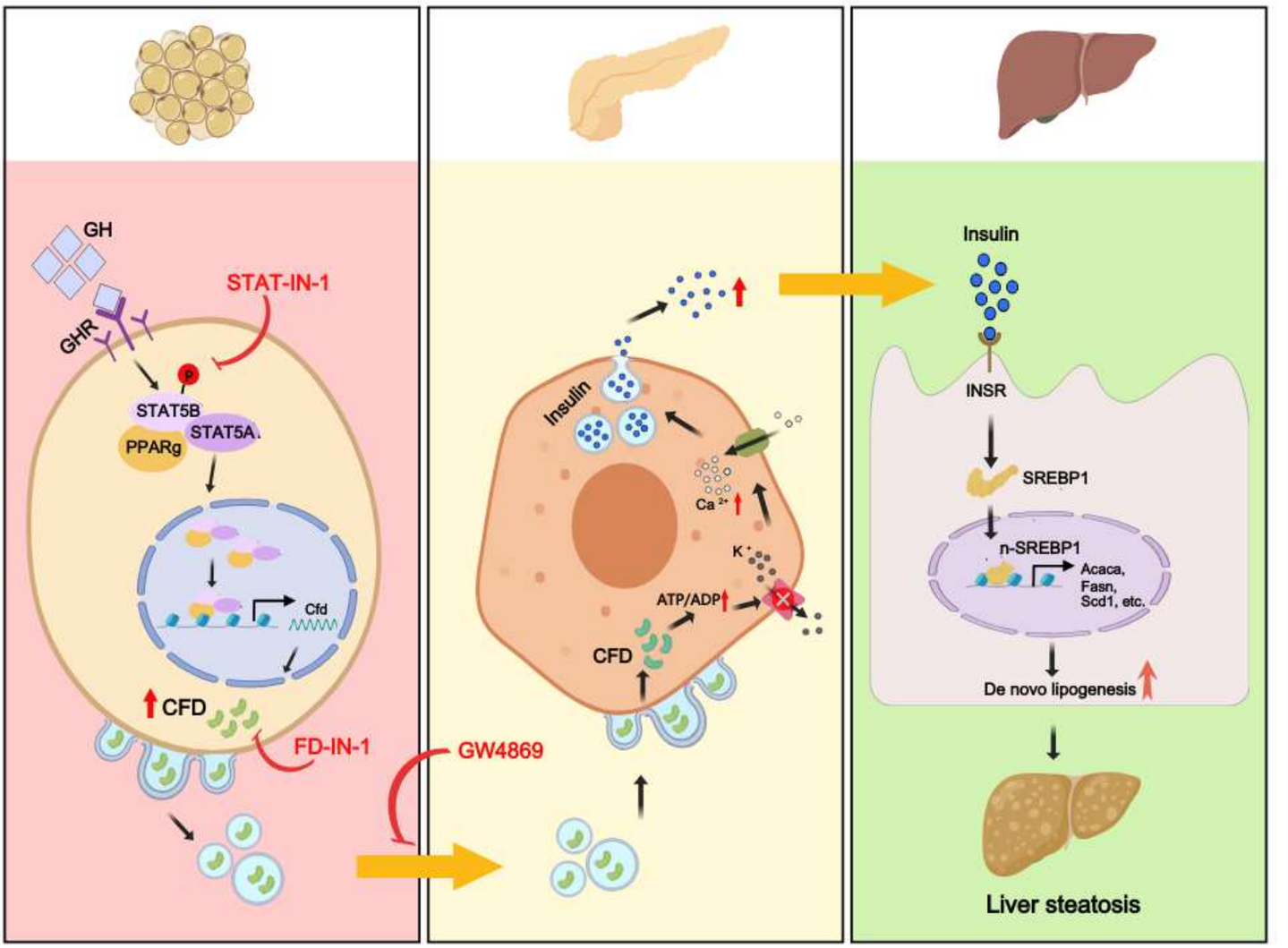

a
Normal
Moderate
Severe
50μm
b
Plasma ALT
U/L
c
Plasma INSULIN
mU/L
d
Plasma CFD
ng/ml
Normal
Moderate
Severe
e
Plasma INSULIN (mU/L)
R=0.68
P<0.0001
Plasma ALT (U/L)
f
Plasma CFD (ng/ml)
R=0.61
P<0.0001
Plasma ALT (U/L)
Plasma CFD (ng/ml)
R=0.71
P<0.0001
Plasma INSULIN (mU/L)
g
Plasma ALT
AUC = 0.899
Acc = 0.878
Youden = 0.806
Plasma INSULIN
AUC = 0.751
Acc = 0.673
Youden = 0.487
Plasma CFD
AUC = 0.888
Acc = 0.796
Youden = 0.672
Combined ROC
Logi
AUC = 0.975
Acc = 0.857
Youden = 0.871
Sensitivity
Specificity
h
1st EVs
2ed EVs
Concentration (particles/ml)
155
139
Normal
Moderate
Severe
Size (nm)
i
1st EV
2ed EV
100nm
j
1st EVs
2ed EVs
Normal
Moderate
Severe
kDa
CFD
TSG101
CANX
40
55
100
k
CFD levels
1st EVs
2ed EVs
Supernatant
ng/ml
Plasma CFD distribution

Fig 10


GH
GHR
STAT-IN-1
P
STAT5B
STAT5A
PPARg
Cfd
CFD
FD-IN-1
GW4869
Insulin
Ca 2+
K+
ATP/ADP
CFD
Insulin
INSR
SREBP1
n-SREBP1
Acaca,
Fasn,
Scd1, etc.
De novo lipogenesis
Liver steatosis

Supplementary Files

This is a list of supplementary files associated with this preprint. Click to download.

- SupplementaryfigsNC5.pdf
- SupplementalTablesWP4.docx
- GelsandBlotsimages.pdf